<center>

Supplementary Information

Electrostatic Fermi Level Tuning in Large-Scale Self-Assembled

Monolayers of Oligo(phenylene-ethynylene) Derivatives

</center>

Xintai Wang,[a' *,†] Ali Ismael,[b*,†] Shanglong Ning,[a ,†] Hanan Althobaiti,[b,c,†] Alaa Al-Jobory,[b,d,†] Jan Girovsky,[a] Hippolyte P.A.G. Astier,[a] Luke J. O'Driscoll,[e] Martin R. Bryce,[e] Colin J. Lambert[b*] and Christopher J. B. Ford[a*]

[a.] Department of Physics, Cavendish Laboratory, University of Cambridge, Cambridge, CB3 0HE, UK: [a'.] School of Information Science and Technology, Dalian Maritime University, Dalian, China.

[b.] Physics Department, Lancaster University, Lancaster, LA1 4YB, UK.

[c.] Department of Physics, College of Science, Taif-University, Taif, KSA.

[d.] Department of Physics, College of Science, University of Anbar, Anbar, Iraq.

[e.] Department of Chemistry, Durham University, Lower Mountjoy, Stockton Road, Durham, DH1 3LE, UK.

*To whom correspondence should be addressed. e-mail: xintaiwang@dlmu.edu.cn, cjbf@cam.ac.uk, c.lambert@lancaster.ac.uk, k.ismael@lancaster.ac.uk

Table of Contents:

Experimental details:

Molecule Synthesis: Synthesis of molecules **1**-**3** and **6** used in this work, and confirmation of their purity, was described in O'Driscoll *et. al.*[1] Known molecules **4**[2] and **5**[3] were prepared in a similar manner as described below; their elemental analysis data is given as evidence of their purity, other characterization was in agreement with that reported previously.

Molecule **4** = OPE2 dithioacetate

4-(Acetylthio)iodobenzene[1] (303 mg, 1.09 mmol, 1.05 eq.) and 4-ethynyl-1-thioacetylbenzene[4] (183 mg, 1.04 mmol, 1 eq.) were dissolved in a mixture of anhydrous THF (16 mL) and anhydrous *N,N*-diisopropylethylamine (DIPEA) (4 mL) in a dry flask under argon and the mixture was degassed (argon, 30 min). CuI (14 mg, 0.07 mmol, 7 mol %) and $Pd(PPh_3)_2Cl_2$ (51 mg, 0.07 mmol, 7 mol %) were added and the mixture was degassed for a further 5 min then left to stir at RT for 20 h. The reaction was then diluted with hexane (25 mL) and passed through a pad of celite to remove insoluble impurities, washing with hexane until the filtrate was colourless. The solvent was removed *in vacuo* to afford crude product which was purified by column chromatography (4 cm Ø, 200 mL SiO_2, eluent: 1:1 CH_2Cl_2/hexane). The resulting off-white solid (118 mg) was further purified by recrystallization from toluene in order to achieve satisfactory elemental analysis data, affording **4** as a white solid (87 mg, 26%). Spectroscopic characterization was in agreement with the literature.[2]

elem.: Anal. Calcd for $C_{18}H_{14}O_2S_2$: C 66.23, H 4.32; Found: C 65.93, H 4.24

Molecule **5** = OPE3 dithioacetate

4-(Acetylthio)iodobenzene[1] (678 mg, 2.44 mmol, 2.05 eq.) and 1,4-diethynylbenzene (150 mg, 1.19 mmol, 1 eq.) were dissolved in a mixture of anhydrous THF (20 mL) and anhydrous DIPEA (5 mL) in a dry flask under argon and the mixture was degassed (argon, 45 min). CuI (23 mg, 0.12 mmol, 10 mol %) and $Pd(PPh_3)_2Cl_2$ (83 mg, 0.12 mmol, 10 mol %) were added and the mixture was degassed for a further 5 min then left to stir at RT for 20 h. The reaction was then diluted with CH_2Cl_2 (25 mL) and passed through a pad of celite to remove insoluble impurities, washing with CH_2Cl_2 until the filtrate was colourless. The solvent was removed *in vacuo* to afford crude product which was purified by column chromatography (5 cm Ø, 250 mL SiO_2, gradient elution from 1:1 to 4:1 CH_2Cl_2/hexane). The resulting white solid (180 mg) was further purified by recrystallization from toluene in order to achieve satisfactory elemental analysis data, affording **5** as a white solid (165 mg, 33%). Spectroscopic characterization was in agreement with the literature.[3]

elem.: Anal. Calcd for $C_{26}H_{18}O_2S_2$: C 73.21, H 4.25; Found: C 73.20, H 4.18

Molecule **5** = OPE3 dithioacetate

4-(Acetylthio)iodobenzene[1] (678 mg, 2.44 mmol, 2.05 eq.) and 1,4-diethynylbenzene (150 mg, 1.19 mmol, 1 eq.) were dissolved in a mixture of anhydrous THF (20 mL) and anhydrous DIPEA (5 mL) in a dry flask under argon and the mixture was degassed (argon, 45 min). CuI (23 mg, 0.12 mmol, 10 mol %) and $Pd(PPh_3)_2Cl_2$ (83 mg, 0.12 mmol, 10 mol %) were added and the mixture was degassed for a further 5 min then left to stir at RT for 20 h. The reaction was then diluted

with CH_2Cl_2 (25 mL) and passed through a pad of celite to remove insoluble impurities, washing with CH_2Cl_2 until the filtrate was colourless. The solvent was removed *in vacuo* to afford crude product which was purified by column chromatography (5 cm Ø, 250 mL SiO_2, gradient elution from 1:1 to 4:1 CH_2Cl_2/hexane). The resulting white solid (180 mg) was further purified by recrystallization from toluene in order to achieve satisfactory elemental analysis data, affording **5** as a white solid (165 mg, 33%). Spectroscopic characterization was in agreement with the literature.[3]

elem.: Anal. Calcd for $C_{26}H_{18}O_2S_2$: C 73.21, H 4.25; Found: C 73.20, H 4.18

Device Fabrication:

The micro-well samples were fabricated on p-doped silicon wafers with a layer of 300 nm native thermal silicon oxide. A standard cleaning method was applied to clean the surface before any photolithography process. The cleaning procedure starts with 5-minute immersion in acetone followed by a 2-minute immersion in propan-2-ol (IPA) to remove acetone residue.

The first photolithography step deposited gold fingers in the central area. A double-layer resist was used to achieve clean lift-off and precise edges. The bottom layer was formed by spinning LOR 5B (7000 rpm, 60 s) and the top layer was formed by spinning positive Shipley 1805 photoresist (S1805, 5500 rpm, 60 s). Directly after coating with LOR 5B the sample was soft-baked for 10 minutes at 180 °C to stabilize the film and improve the adhesion. After spinning the S1805, the samples were baked at 110 °C for 2 minutes. The UV exposure time was 7.5 seconds; afterwards, the sample was developed in MICROPOSIT MF-319 developer for 20 seconds and then rinsed in DI water. Once the finger pattern had been developed, 5 nm titanium and 20 nm gold were evaporated onto the surface. SVC-14 positive photoresist stripper was used to lift off the unwanted metal.

A series of micro-wells was formed on top of the fingers by selectively etching holes in a 25 nm layer of aluminium oxide. First, atomic-layer deposition was used to deposit a high-quality layer of aluminium oxide with a precise thickness. Using photolithography, holes were opened up in the resist and buffered hydrofluoric acid was then used to etch through the aluminium oxide below, stopping at the gold. Once the micro-wells were formed, S1805 was spun on, to protect the common contacts and gate electrode, and it was removed over the micro-well region using photolithography to allow molecule assembly on the unprotected gold.

A flow chart of device fabrication is shown below (Fig. S1):
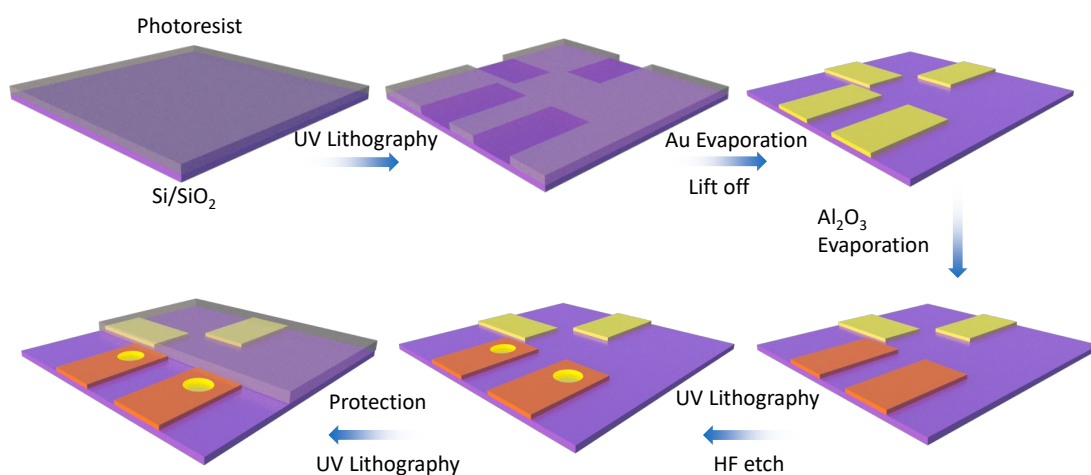
Fig. S1. Flow chart of micro-well device fabrication.

Device pre-treatment:

Each device after fabrication was washed with DI water (R>10 MΩ) several times to eliminate any possible metal/salt contaminants, then immersed in hot dimethylformamide (DMF, Sigma-Aldrich, 99.8%, 90 °C) for 20 minutes to wash off organic contaminants. The device after washing was rinsed in ethanol 3-4 times, and then rinsed in DMF before being put into the chosen solution of molecules to form a SAM.

SAM growth:

We modified the standard method for SAM growth. The solution of molecules was prepared by dissolving target molecules in DMF with a concentration of 1 mM, and the solution was ultra-sonicated for 10 minutes to dissolve the molecules completely. The device after pre-treatment was immersed in this solution for 30 minutes, washed with DMF, ethanol (EtOH), and IPA 3-4 times and re-immersed in the solution. This process was repeated 4 to 5 times, and after that, the device was immersed in the solution for 24-48 hours for SAM growth and self-organisation. Our experiments suggest this type of 'stepwise' self-assembly helps to cure the pinholes in the SAM and decreases the possibility of short circuits. The device after SAM growth was rinsed with DMF, ethanol and IPA 3-4 times to eliminate physisorbed molecules, and dried at 30 °C. Finally, the S1805 layer protecting the contacts was washed off with acetone and then IPA.

Graphene transfer:

Single-layered graphene on copper (Graphene supermarket, Graphene on 1 side) was used in this work. The copper etching procedure followed the standard recipe for graphene transfer:[5] 0.1 M ammonium persulfate (APS) was dissolved in water as etchant solution. 4% poly(methyl methacrylate) (PMMA) was spin coated on copper with graphene (6000 rpm, 1 min) as a protection layer, and incubated at 150 °C for 1 minute to allow solvent evaporation. After heating, PMMA/graphene/Cu was transferred into the etchant solution for Cu etching. The etching

process takes 18-24 hours. After copper etching, the graphene was transferred into clean DI water for 6 times to wash off remaining APS, and the PMMA-protected graphene was transferred onto our device with SAM by 'fishing'.

The device after graphene transfer was incubated in high vacuum (10^{-7} mbar) for 24 hours to remove residual water. After this drying stage, the PMMA was washed off by immersing the device in acetone, and rinsing under acetone gently with further acetone from a glass pipette. This procedure was repeated several times, and the device after rinsing was immersed in acetone overnight to eliminate PMMA residue. Below is a flow chart for graphene transfer:
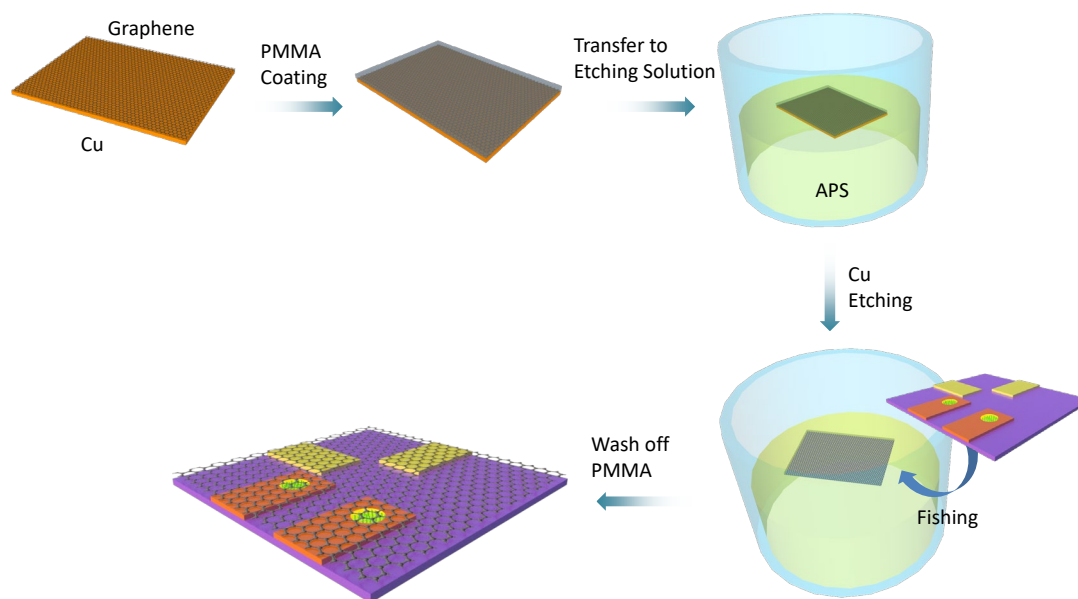
Fig. S2. Flow chart of transferring graphene on top of a micro-well device

Graphene patterning:

The device after PMMA removal was coated with photoresist (S1805) by spin coating, and dried in high vacuum overnight. UV-lithography was used to pattern graphene stripes covering each set of micro-wells, and the un-protected graphene was removed with an RF (Radio Frequency) asher to avoid short-circuits.

The flow chart below (Fig. S3) shows these steps:
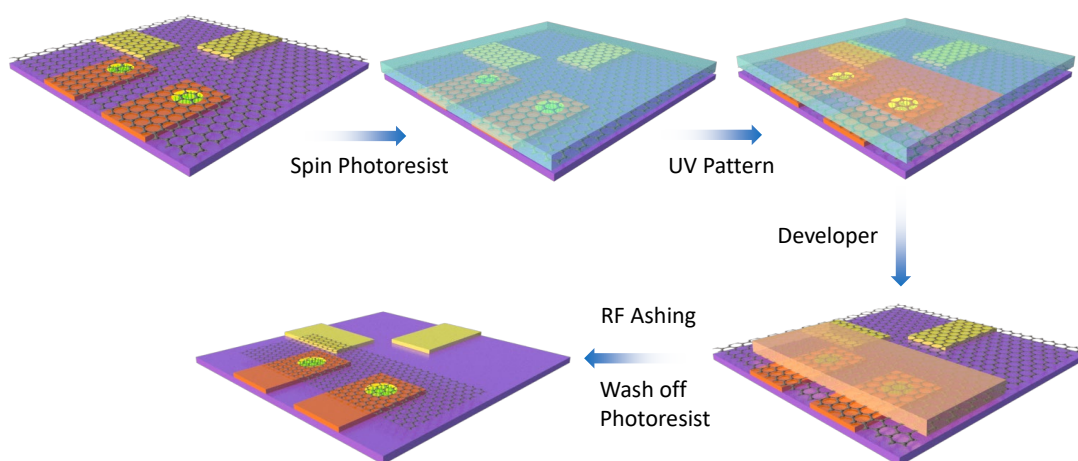
Fig. S3. Flow chart of etching off unwanted graphene parts

Electrical Measurement

The device after fabrication was wire-bonded to a leadless chip carrier, keeping the temperature at 35°C. The bias voltage between source and drain (V_{SD}) was generated by a Keithley 2400 SMU.

The differential conductance (dI/dV) was obtained using a lock-in amplifier (SR830). A homemade DC/AC mixer was used to mix the DC voltage generated from the Keithley 2400 SMU (floating) and the AC voltage generated from the SR830's internal oscillator (grounded, 10 mV amplitude, 127 Hz frequency). The current was converted to a voltage signal using a Femto DLPCA 200 current pre-amplifier and measured by the SR830 lockin amplifier.

For each type of molecule, at least 2 independent batches of samples were prepared (using the same recipe) to assess reproducibility and detect unwanted one-off effects (contamination, low-quality graphene, bad SAM etc.). On occasions when data showed signs of bad SAM or graphene quality (many shorts or low Au/graphene/Au conductance), or the measured conductances had large disagreement with each other, more batches were prepared and measured.

Ionic liquid gating

A small droplet of ionic liquid diethylmethylammonium bis(trifluoromethylsulfonyl)imide (DEME-TFSI, Sigma Aldrich, >98.5%, ~50 µL) was dropped onto the device. The device was checked in an optical microscope to ensure all the micro-wells and gate electrodes were covered by the ionic liquid. The leakage current between the gate and common contacts was checked before and after adding the ionic liquid drop as shown in Fig. S4.

A second Keithley 2400 SMU was used to apply a series of gate voltages in the range where there was almost no leakage current. At each gate voltage, the junction was stabilized for 240 seconds, and then the SD voltage was applied and electrical transport was measured as described in the Electrical Measurement section (scan rate 300 mV/s). To establish that the molecules do not desorb from the electrodes, three IV curves were measured at each gate voltage for several cycles and the current remained constant; if desorption was occurring a rapid increase in current would be expected because of the short circuit between gold and graphene electrodes.. *I-V* characteristics of the junction at zero gate voltage were measured before and after applying the series of gate voltages, and also compared with the *I-V* curve before addition of the ionic liquid, to ensure that the ionic liquid and gate voltage did not destroy the junction (Fig. S8).

XPS measurement

5 nm titanium and 20 nm gold were evaporated onto a Si/SiO_2 substrate. The prepared Au sample was spin coated with S1805 photoresist, exposed under UV light (without shadow mask) and developed by the developer. The process was the same as mentioned in the Device Fabrication section, and was used to ensure that the photolithography process on the gold surface (mentioned in the Device Fabrication section) did not impact the SAM growth.

The pre-treatment and SAM growth procedure for XPS samples was the same as in the 'device pre-treatment' and 'SAM growth' sections.

X-ray photoelectron spectroscopy (XPS) analysis was carried out using a customized NAP-XPS spectrometer from SPECS Surface Nano Analysis GmbH (Berlin, Germany) that allows the possibility of doing measurements at pressures lower then 10^{-5} mBar. The instrument was operated in the fixed analyser transmission mode, a monochromatic Al-Kα source (1486.74 eV) and 90 W was used. Survey and narrow scans were acquired using pass energy of 20 eV. For all samples, 3 survey scans were recorded using 1 eV steps and dwell time of 0.1 s. For narrow scans of C, Au, O, the number of scans was 2, using step size of 0.1 eV and dwell time of 0.5 s. For narrow scans of N and S the step size used was 0.05 eV, 0.5 s dwell time and 10 and 20 scans were recorded, respectively. The number of scans of C, Au, N, S for reference samples was 2 using the corresponding step sizes and dwell times as for the rest of the samples.

Raman Measurement

CVD graphene from the same batch as that used for device fabrication was transferred after copper etching onto a SiO_2/Si substrate for Raman characterisation using a Renishaw Raman system.

AFM Characterisation

AFM characterisation was carried out in an MFP-3D AFM System (Asylum/Oxford Instruments). The topography of all the images was obtained using a Multi75-G tip from Budget Sensors in tapping mode.

Film thickness estimation

The thickness of the SAMs was estimated from the attenuation of Au spectra[6-8], using

$$d = \lambda \ln\left(\frac{I_{Au}}{I_{SAM}}\right),$$

where d is the thickness of the film, λ the attenuation length (4.2 nm for OPE-based molecules), I_{Au} the Au signal of a clean gold surface (treated in the same way as the SAM sample, but immersed in DMF solution without molecules), I_{SAM} the Au signal of gold after SAM deposition (with a sample analyser angle of 90°).

The estimated SAM thickness for different molecules is listed in Table S3, and the XPS signal of Au spectra is shown in Fig. S6.

Micro-well size estimation

High-resolution images of the micro-well were taken in an optical microscope and the etched area was estimated by counting pixels from a home-made python program using these images. An AFM was used to scan some of the wells from different preparation batches to confirm the accuracy of this estimation method (Fig. S13, Table S3).
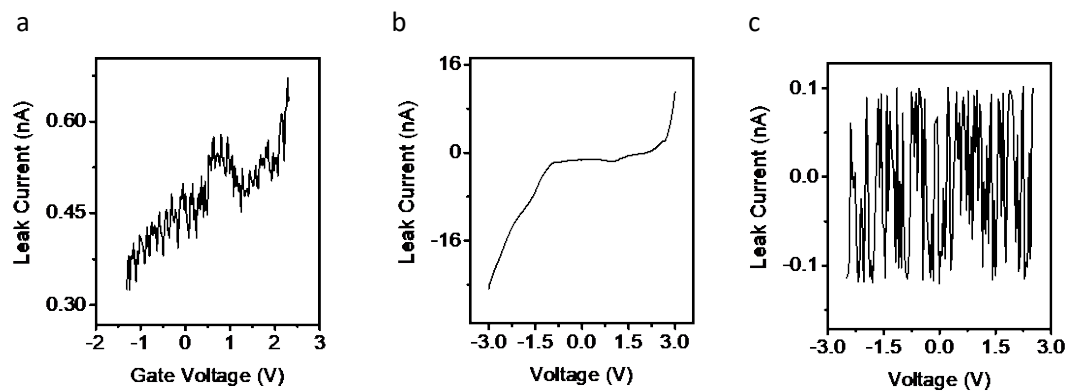
Fig. S4. A typical example of gate-drain leakage current of an ionic liquid droplet for gate voltages from −1.3 to +2.3 V (a) and −3 to +3V (b), and the leakage current without ionic liquid in the voltage range −2.5 to +2.5 V (c). A small positive offset was observed in Fig. S4(a) due to the charge gradient induced by the ionic liquid.
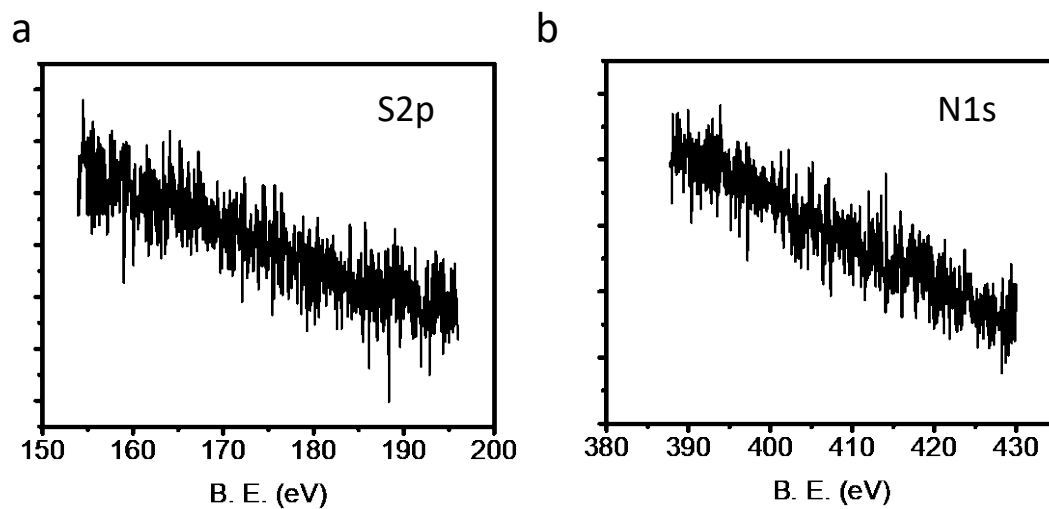
Fig. S5. XPS measurements of the S2p and N1s spectra for a clean gold surface.
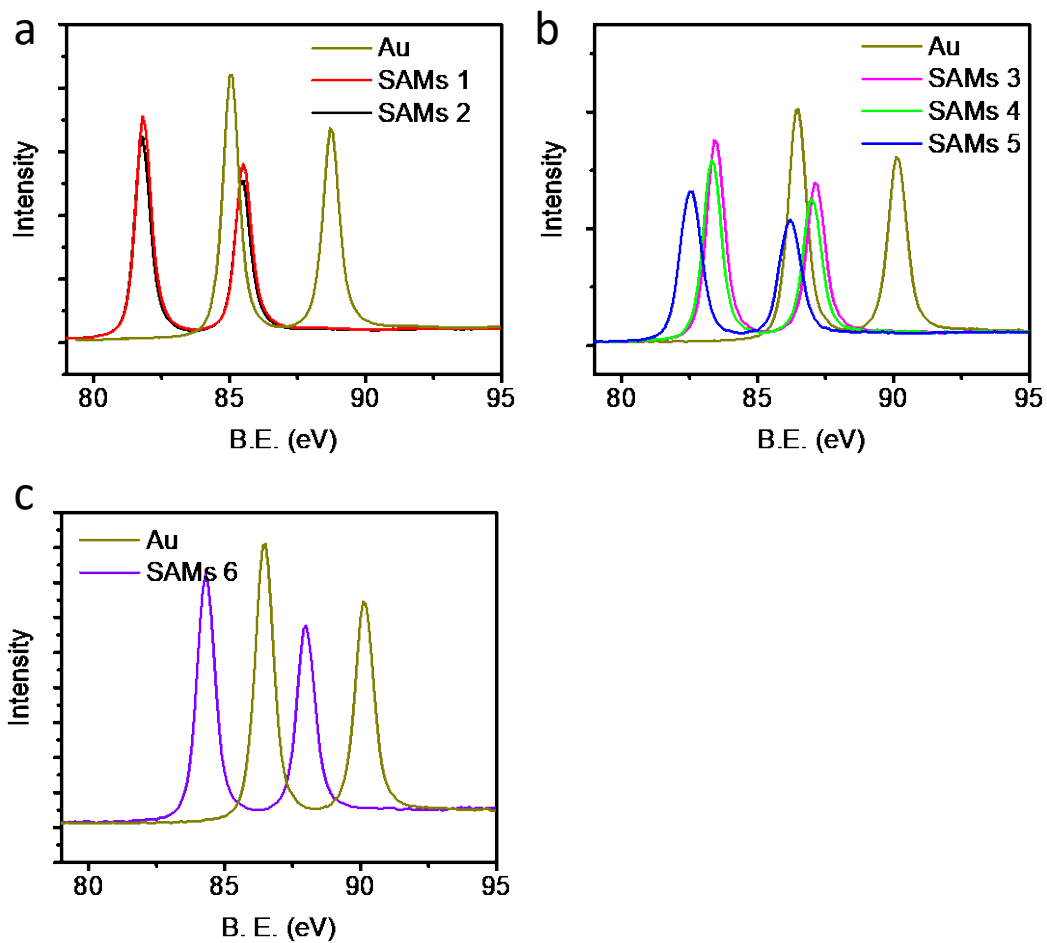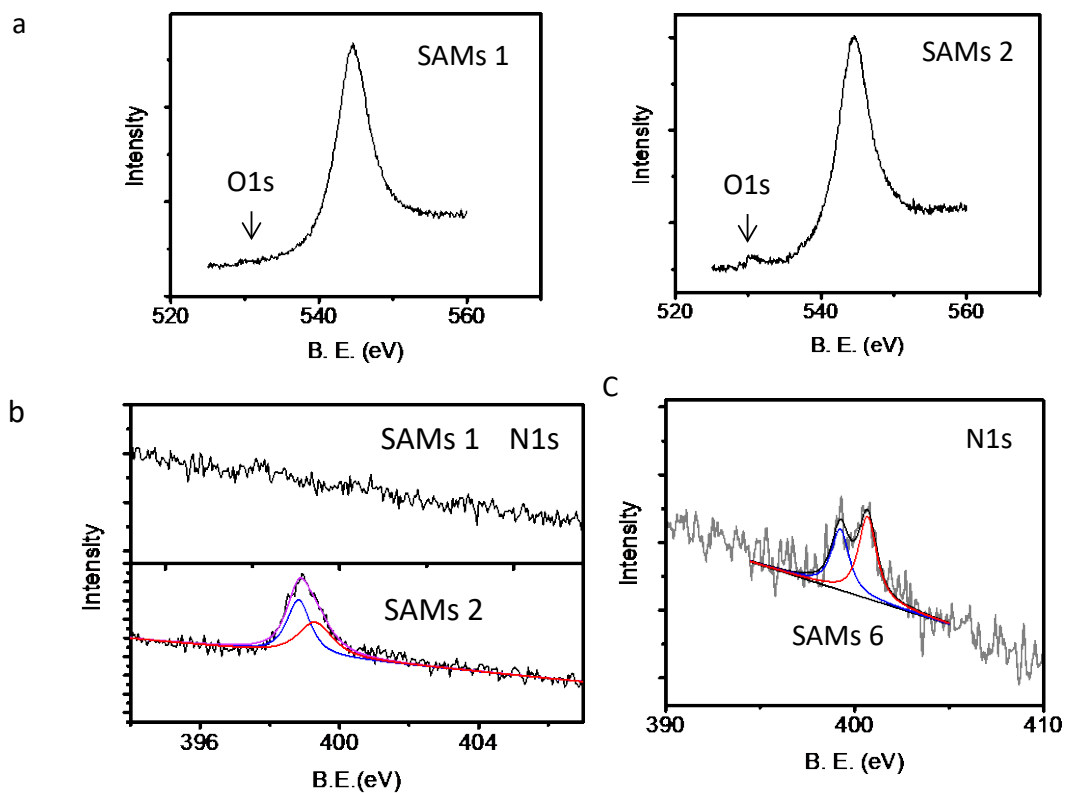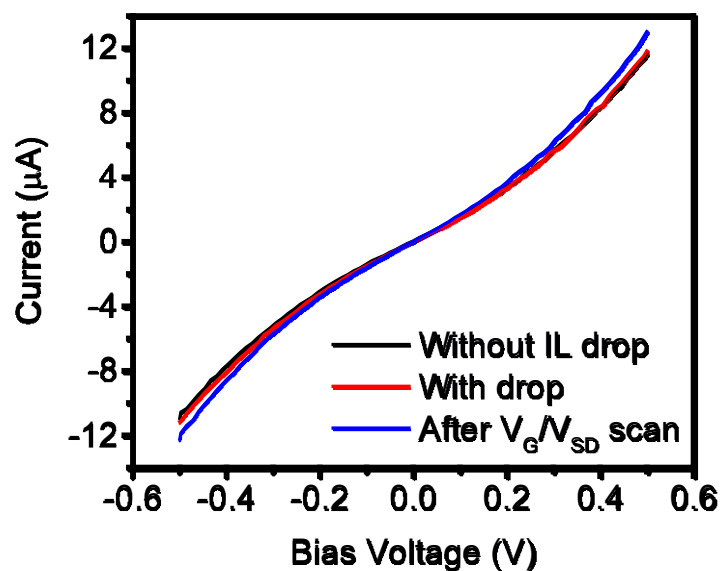
Fig. S6. XPS Au spectra of clean gold and gold with SAMs **1-6** as labelled.

Fig. S7. XPS result of O1s (a) spectra for SAMs **1** (left) and SAMs **2** (right), and N1s spectra of SAMs **1** and **2** (b) and **6** (c).

Fig. S8. A typical example of an *I-V* curve of a molecular junction with SAM **1** at zero gate voltage, before (black) and after (red) adding the ionic liquid (IL), and (blue) after the series of V_{SD} sweeps at different gate voltages to map conductance *vs* V_{SD} and V_{gate} (waiting 30 minutes after the gate voltage was swept back to 0 V).
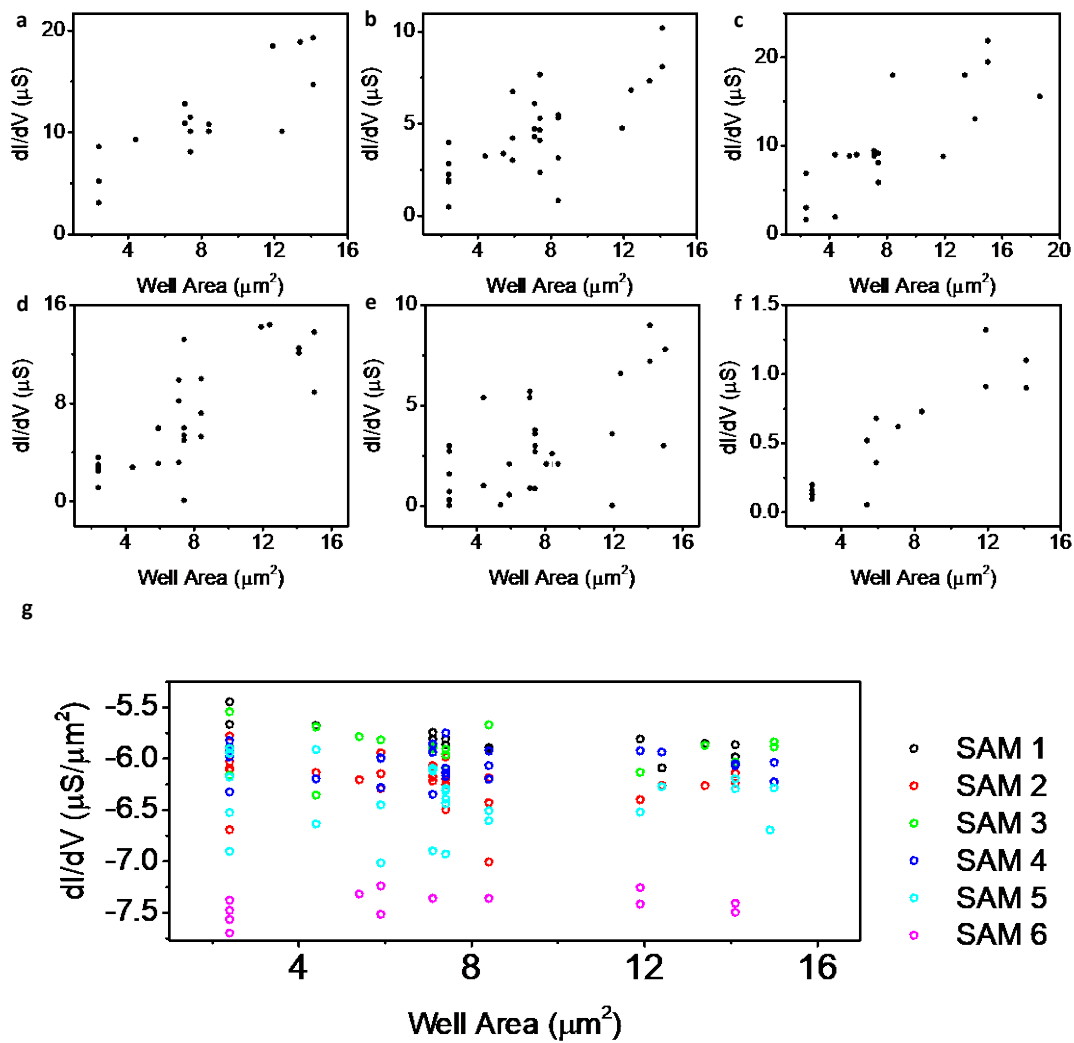
Fig. S9. Conductance at zero bias (a-f) and conductivity (g) of SAMs **1-6** vs. well area.
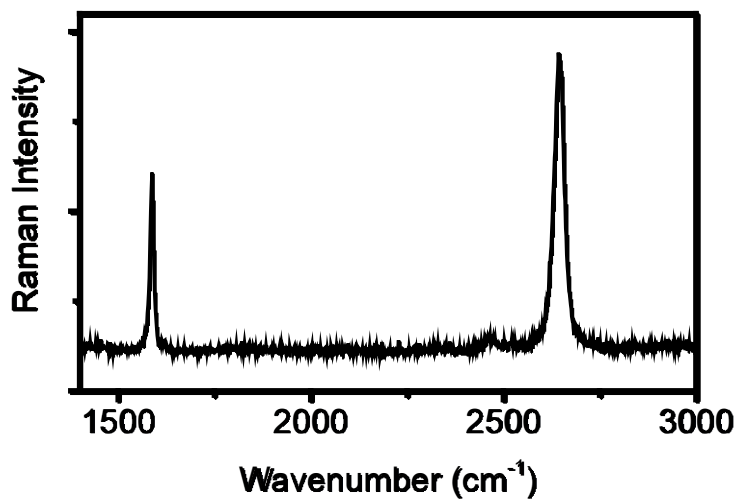
Fig. S10. Raman spectra of graphene used in this work, transferred on to a Si/SiO₂ substrate.
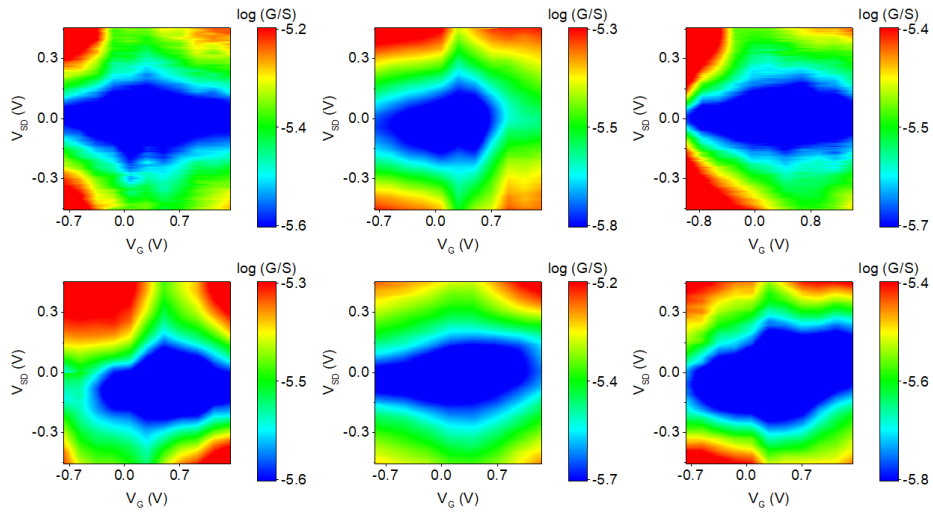
a

b
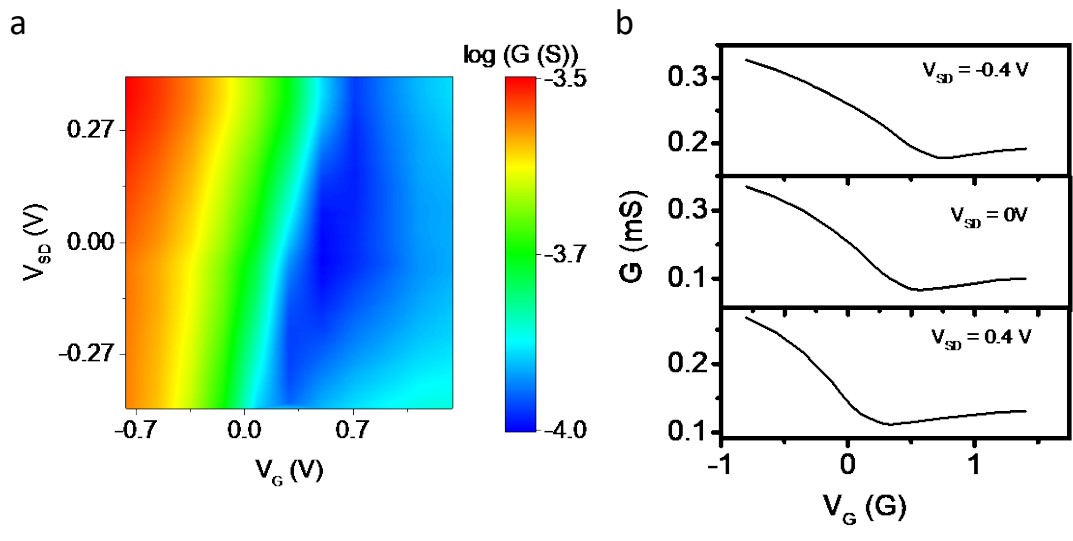
Fig. S11. (a) Plot of log(G) *vs* V_G and V_{SD} for an Au/Graphene/Au junction. (b) Plot of the conductance of graphene *vs* V_G at three different SD voltages.
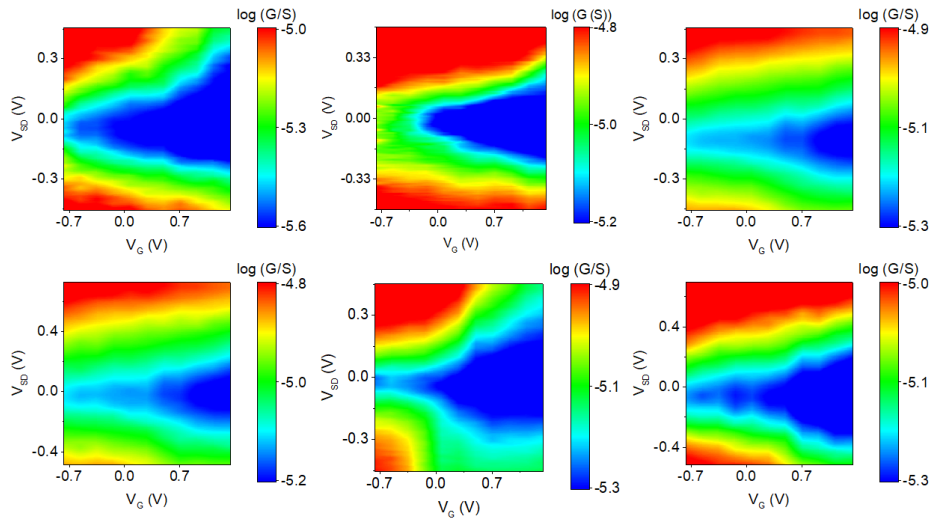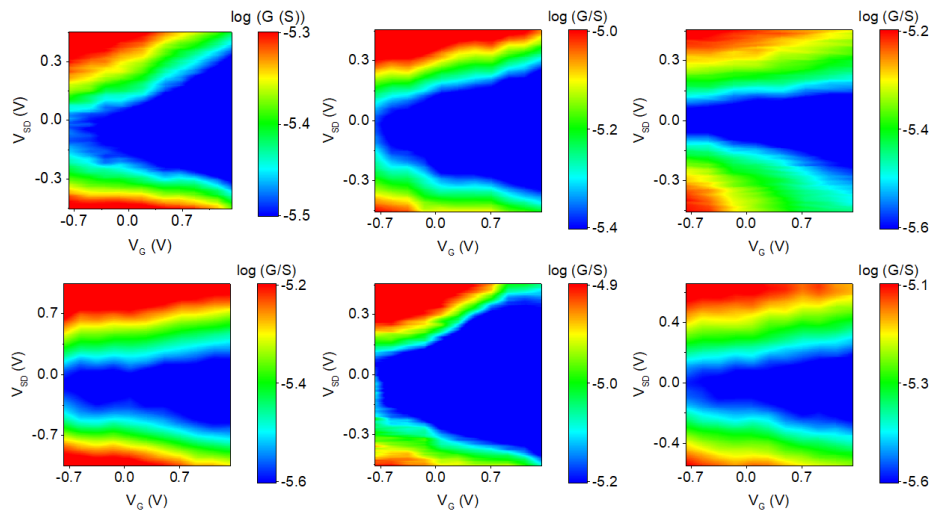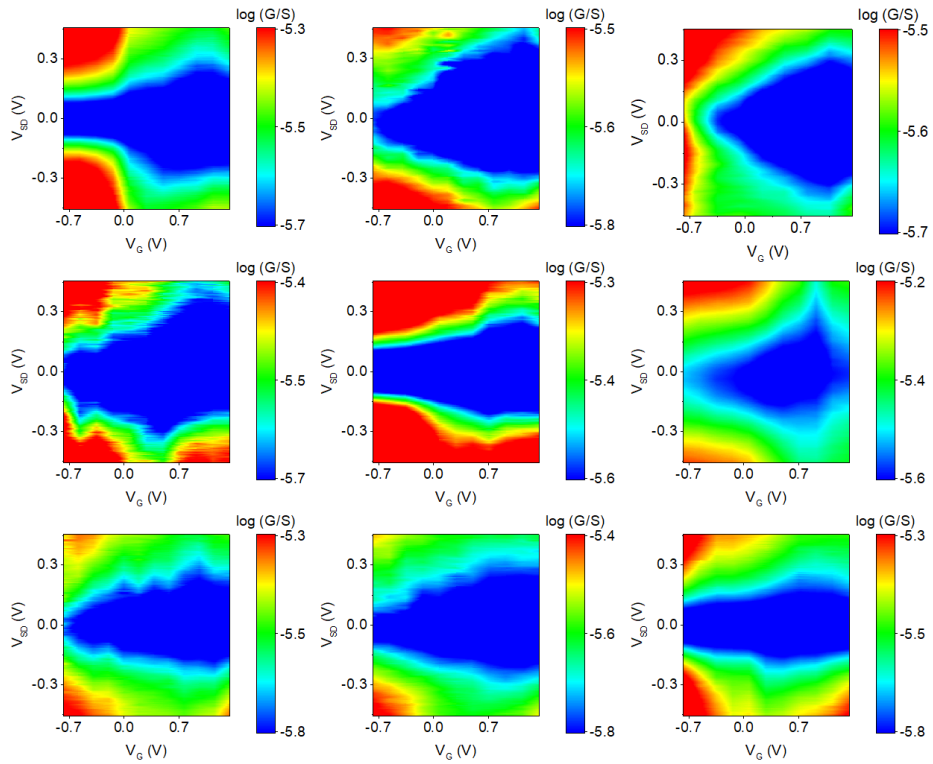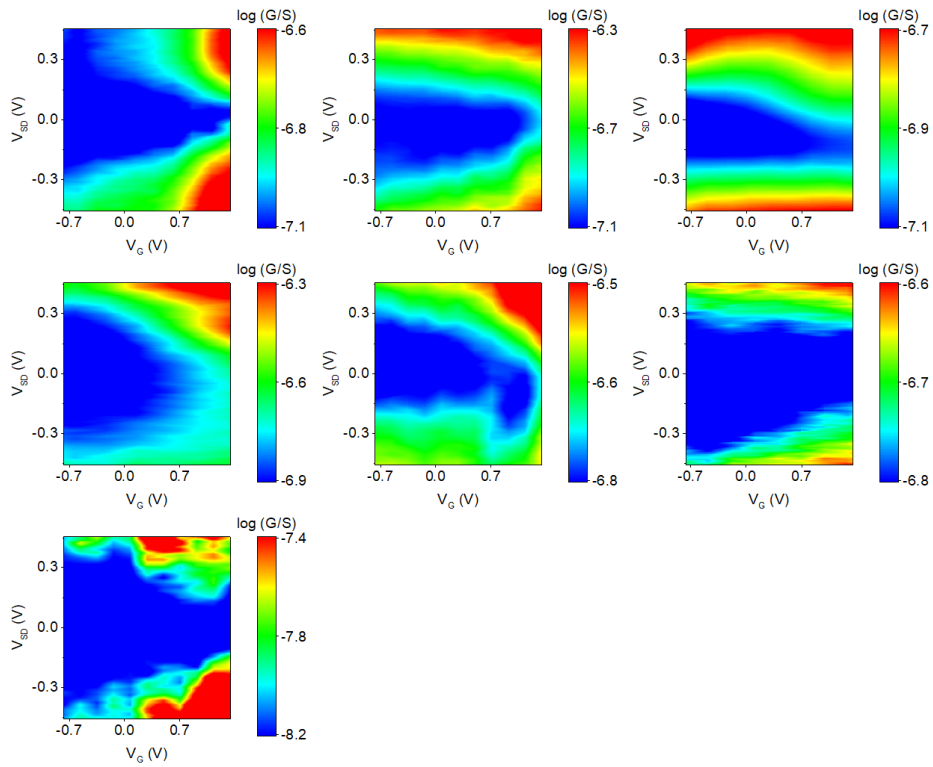
SAM **1**:
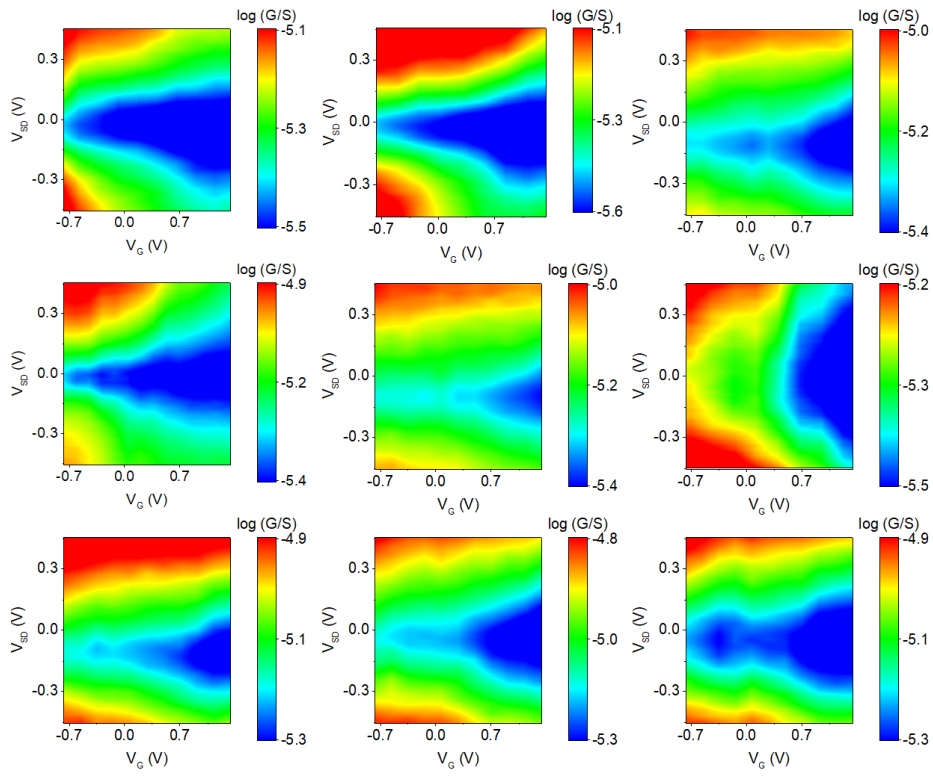
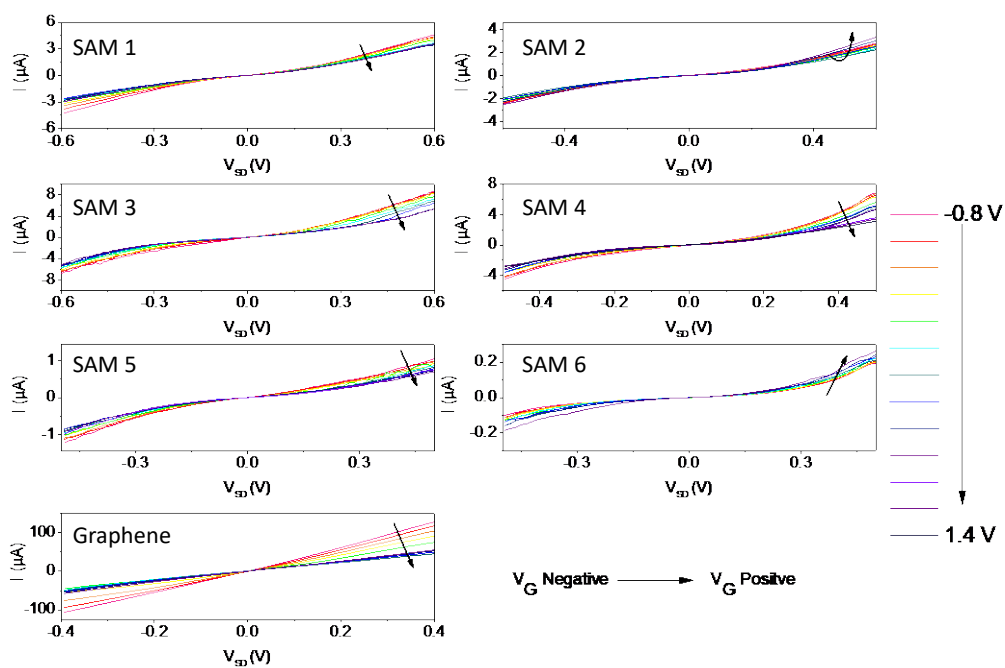SAM **2**:

SAM **3**:

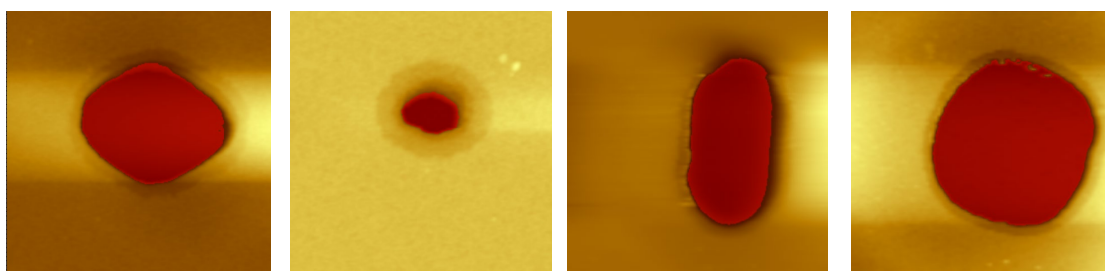SAM **4**:

SAM **5**:

SAM **6**:

Fig. S12. *G* vs *V*$_{SD}$ and *V*$_{G}$ for many different junctions in two or more fabrication batches for each of SAMs **1-6**, showing reproducibility of the observed dependences.

Fig. S13. *I-V* curves for Au/SAM **1-6**/Graphene and Au/Graphene junctions at different gate voltages. The arrows show how the curves change with increasing V_G.

Fig. S14. Examples of AFM scans of microwells (red region) to measure the areas.
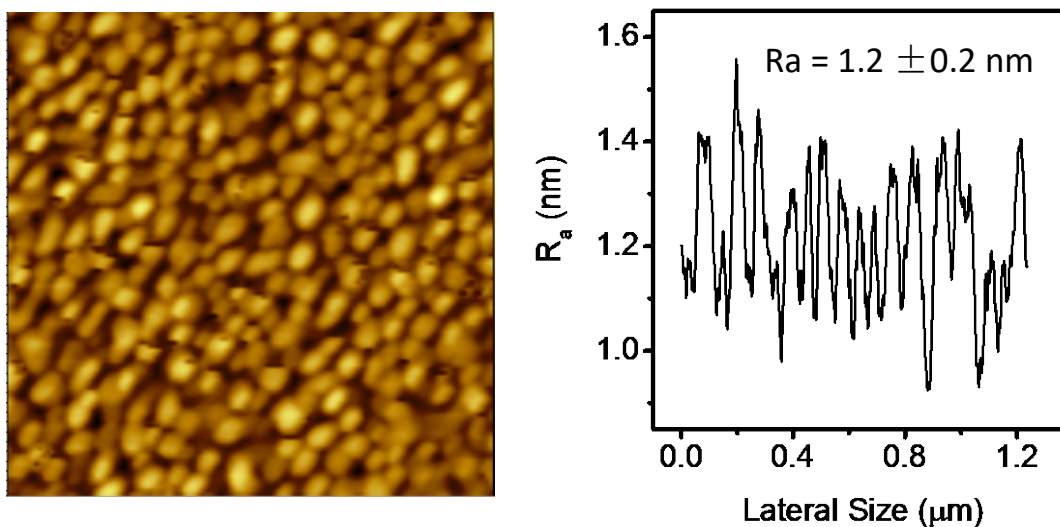
Fig. S15. An example of gold roughness inside a well after device fabrication, measured using an

AFM. In total, 9 different wells from 3 devices prepared from different batches were measured, and the average roughness was 1.2±0.2 nm.

SAM	Survive	Shorted	Open
1	17/32 (53%)	14/32 (44%)	1/32 (3%)
2	48/64 (75%)	15/64 (23%)	1/64 (2%)
3	18/32 (56%)	14/32 (44%)	0/32 (0%)
4	19/32 (59%)	13/32 (41%)	0/32 (0%)
5	19/32 (59%)	13/32 (41%)	0/32 (0%)
6	21/64 (33%)	41/64 (64%)	2/64 (3%)

Table S1. Survival rate of devices based on SAMs **1-6**

SAM	No. measured with gate control	V_G with G_{min} (V)	Standard deviation (V)
1	9	>1.4	-
2	7	0.22	0.08
3	6	>1.4	-
4	7	>1.4	-
5	9	1.05	0.15
6	6	<-0.8	-

Table S2. Gate voltage at which the conductance minimum occurs for SAMs **1-6.**

Device Batch	Estimated Area (μm^2)	AFM Area (μm^2)	Accuracy (%)
1	7.4	7.1	96
1	5.9	5.1	88
1	2.4	1.7	71
2	7.4	7	95
2	11.9	11.6	97
2	2.4	1.1	46
3	7.4	6.9	93
3	7.1	6.9	97
3	5.9	5.2	88
4	2.4	1.3	54
4	7.4	7.2	97
4	8.4	8.3	99

Table S3. Well area of device estimated via AFM and pixel counting

Molecule	Average Thickness	Estimated Tilt Angle (°)
1	0.8 nm	42
2	1.05 nm	42[1]/68[2]
3	0.7 nm	42[1]/16[2]
4	1.1 nm	43
5	1.7 nm	45
6	0.8 nm	40

Table S4. Film thickness information extracted from XPS Au spectra. [1]SAM with binding geometry of motif a; [2]SAM with binding geometry of motif b.

Film Thickness Estimation:

The average thickness of a film was estimated by XPS as mentioned in the previous section, and then the tilt angle was estimated via the equation[9]

$$\theta = \sin^{-1}\left(\frac{d}{d_\mathrm{m}}\right)$$

with θ the tilt angle, d the average film thickness, and d_m the molecular length.

For SAMs **2** and **3**, we assume the tilt angle of motif a is similar to SAMs **1** and **4** because they have the same anchor group and backbone structure, and the SAM thickness of SAM binding with motif b, $d_\mathrm{motif\ b}$, was estimated via equation:

$$d_\mathrm{motif\ b} = \frac{d - \alpha \times d_\mathrm{motif\ a}}{\beta} \ ,$$

with $d_\mathrm{motif\ a}$ the film thickness of molecule bonded with motif a, d the average thickness, α and β the percentage of molecule bonded with motifs a and b estimated via XPS sulphur spectra. The tilt angle of molecules in motif b was then estimated to be

$$\theta = \sin^{-1}\left(\frac{d_\mathrm{motif\ b}}{d_\mathrm{m}}\right) \ .$$

Theoretical details

2. DFT and Transport Calculations

2.1 Optimized DFT Structures of Isolated Molecules

Using the density functional code SIESTA,[10, 11] the optimum geometries of the isolated molecules **1**-**6** were obtained by relaxing the molecules until all forces on the atoms were less than 0.01 eV / Å as shown in Fig. S16. A double-zeta plus polarization orbital basis set, norm-conserving pseudopotentials, with an energy cut-off of 250 Rydbergs, defined on the real-space grid was used and the local-density approximation (LDA) was chosen to be the exchange-correlation functional. We also computed results using GGA and found that the resulting transmission

functions were comparable with those obtained using LDA.[12, 13]
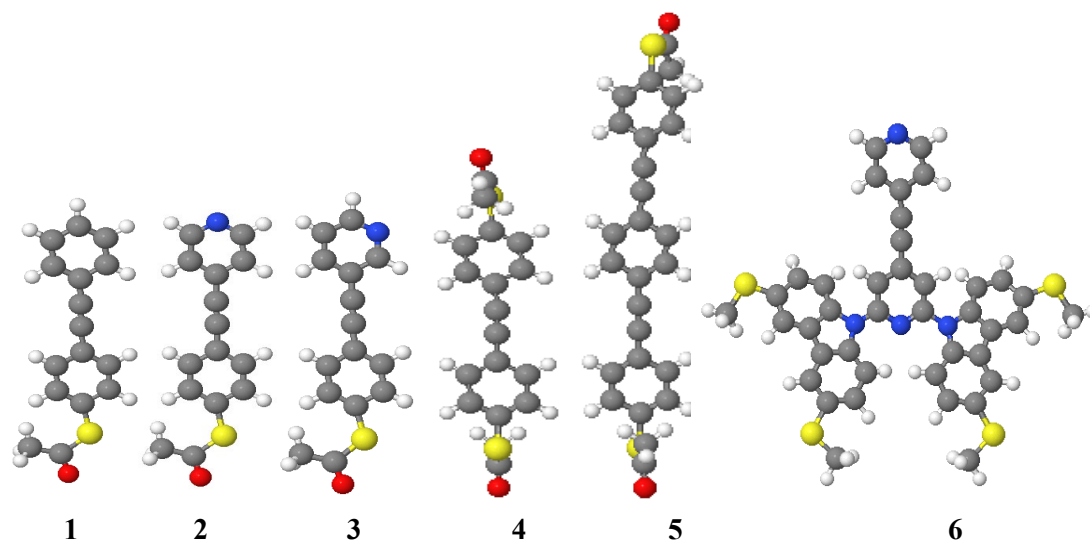
Fig. S16. Fully relaxed isolated molecules **1-6**. Key: C = grey, H = white, O = red, S = yellow, N=blue.

2.2 Frontier orbitals of the molecules

The plots below (Figs. S17–S22) show isosurfaces of the HOMO, LUMO, HOMO–1 and LUMO+1 of isolated molecules **1-6** along with their energies.

$E_F = -2.83$ eV

HOMO E = −4.41 eV

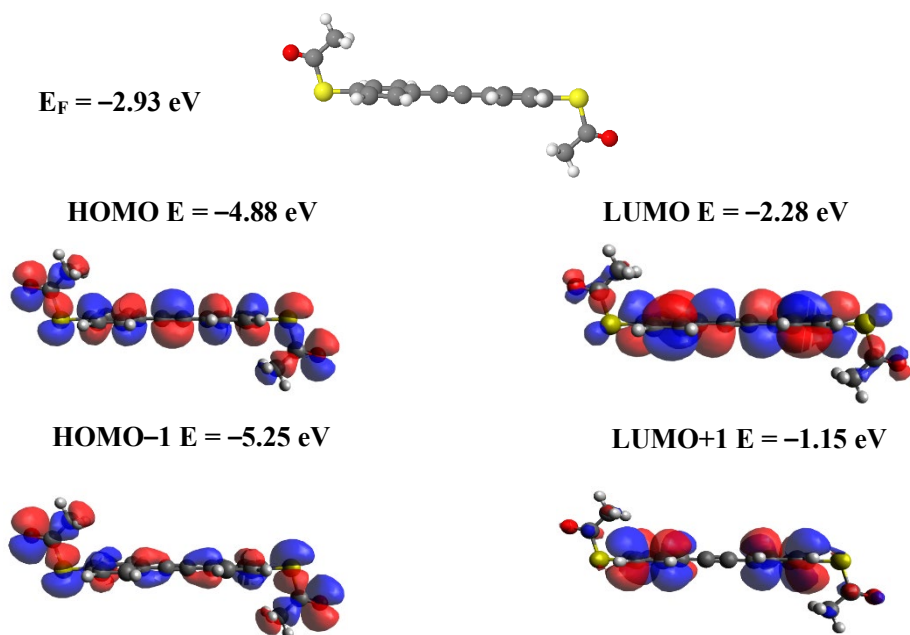LUMO E = −2.12 eV

HOMO–1 E = −4.97 eV

LUMO+1 E = −1.26 eV
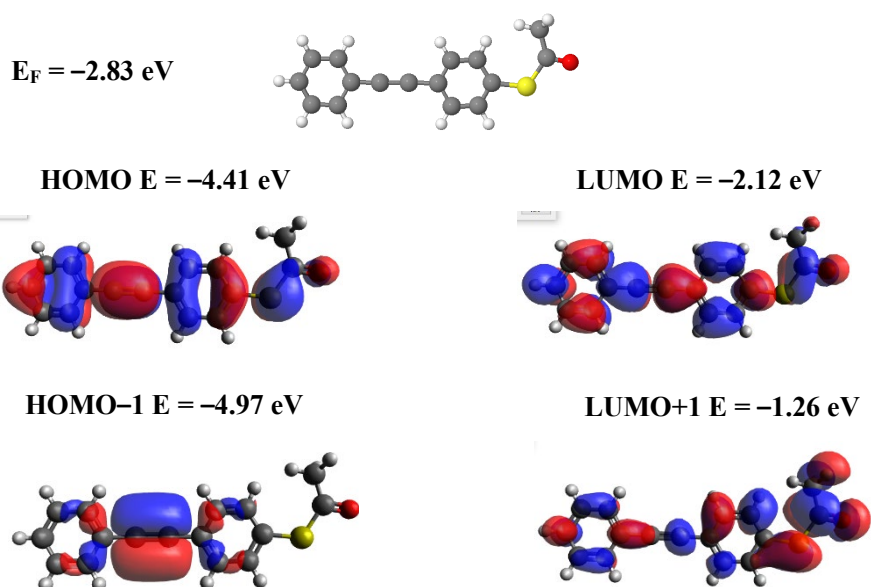
Fig. S17. Wave function for **1**. Top panel: Fully optimized geometry of **1**. Lower panel: HOMO, LUMO, HOMO–1 and LUMO+1 along with their energies.

$E_F = -3.09$ eV

HOMO E = −4.83 eV   **LUMO E = −2.11 eV**

HOMO−1 E = −5.08 eV   **LUMO+1 E = −1.25 eV**
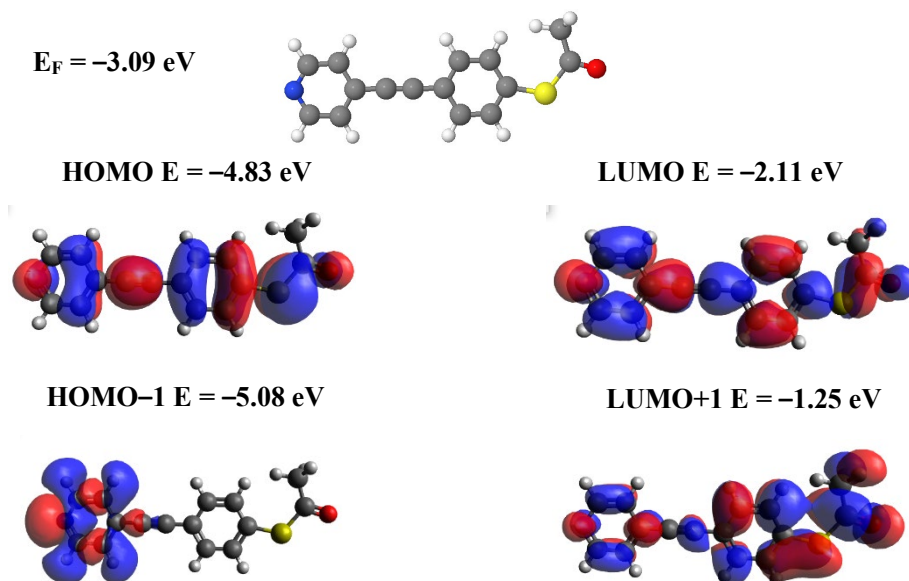
Fig. S18. Wave function for **2**. Top panel: Fully optimized geometry of **2**. Lower panel: HOMO, LUMO, HOMO–1 and LUMO+1 along with their energies.

$E_F = -3.10$ eV

HOMO E = −4.71 eV   **LUMO E = −2.00 eV**

HOMO−1 E = −5.10 eV   **LUMO+1 E = −1.20 eV**
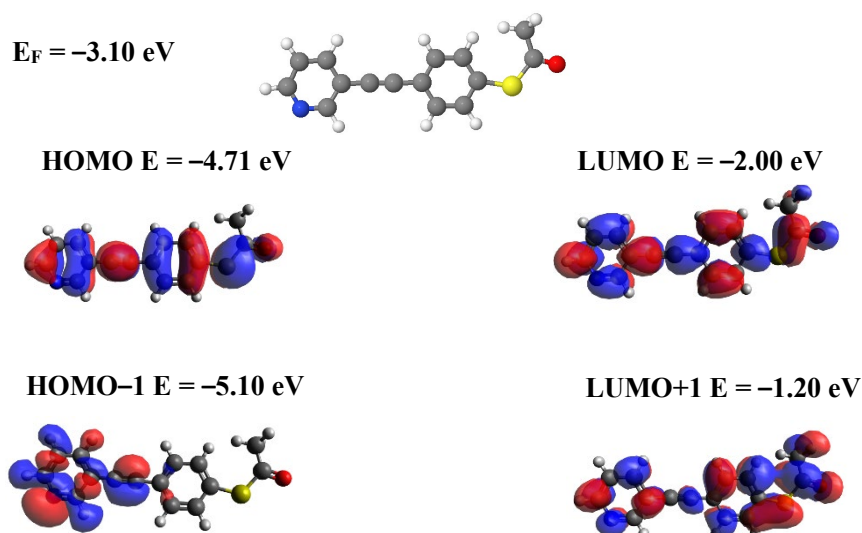
Fig. S19. Wave function for **3**. Top panel: Fully optimized geometry of **3**. Lower panel: HOMO, LUMO, HOMO–1 and LUMO+1 along with their energies.

E_F = −2.93 eV

HOMO E = −4.88 eV

LUMO E = −2.28 eV

HOMO−1 E = −5.25 eV

LUMO+1 E = −1.15 eV

Fig. S20. Wave function for **4**. Top panel: Fully optimized geometry of **4**. Lower panel: HOMO, LUMO, HOMO–1 and LUMO+1 along with their energies.

E_F = −3.96 eV

HOMO E = -4.72 eV

LUMO E = −2.46 eV

HOMO−1 E = −5.11 eV

LUMO+1 E = −1.65 eV
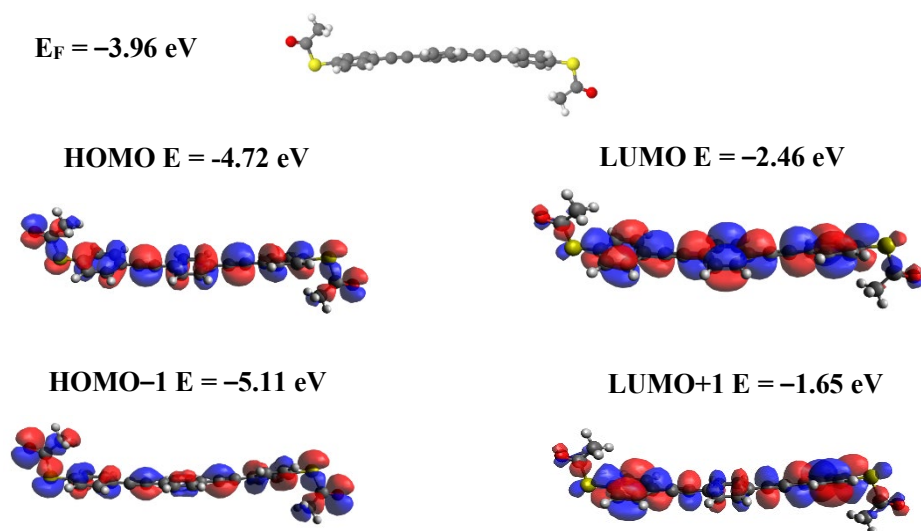
Fig. S21. Wave function for **5**. Top panel: Fully optimized geometry of **5**. Lower panel: HOMO, LUMO, HOMO–1 and LUMO+1 along with their energies.

E_F = −3.37 eV

HOMO E = −4.07 eV

LUMO E = −2.60 eV

HOMO−1 E = −4.21 eV

LUMO+1 E = −1.63 eV
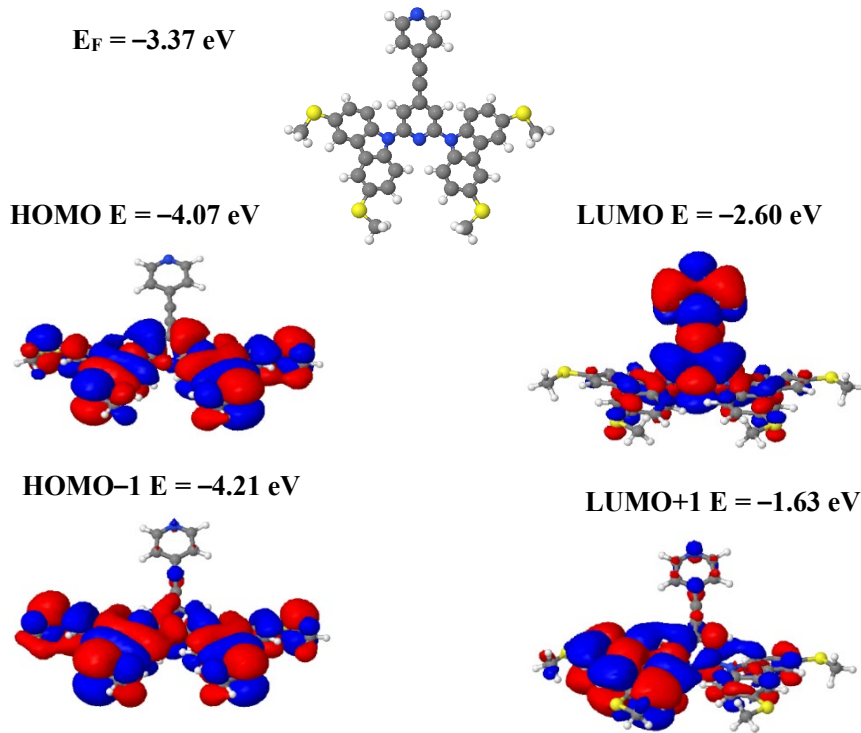
Fig. S22. Wave function for **6**. Top panel: Fully optimized geometry of **6**. Lower panel: HOMO, LUMO, HOMO−1 and LUMO+1 along with their energies.

2.3 Binding energies of molecules on graphene and gold

To calculate the optimum binding distance between the anchor groups and electrodes, we used DFT and the counterpoise method, which removes basis-set superposition errors (BSSE). The binding distance z is defined as the distance between the top or bottom surface and the anchor group (see the black double-arrow on the right panel of Figs. S23-S28).

We define one of the compounds **1-6** as entity A and the single-layer graphene (SLG) or gold electrode as entity B. The ground-state energy of the total system is calculated using SIESTA and is denoted E_{AB}^{AB}. The energy of each entity is then calculated in a fixed basis, which is achieved using ghost atoms in SIESTA. Hence, the energy of the individual molecule **1-6** in the case of the fixed basis is defined as E_{A}^{AB} and for the graphene/gold as E_{B}^{AB}. The energy difference $\Delta(z)$ between the isolated entities and their total energy when placed a distance z apart is then calculated using the following equation:

$$\text{Energy difference} = \Delta(z) = E_{AB}^{AB} - E_{A}^{AB} - E_{B}^{AB} \quad . \qquad \text{(S1)}$$

The energy differences are shown as a function of separation z in Figs. S23-S28 for molecules **1-6** with the equilibrium distance z, corresponding to the minimum energy difference to the electrode, tabulated in Table S5. Here, the energy difference has been calculated for two different contact electrodes. The top contact is graphene-molecule (Gr-M), whereas the bottom contact is gold-molecule (Au-M).
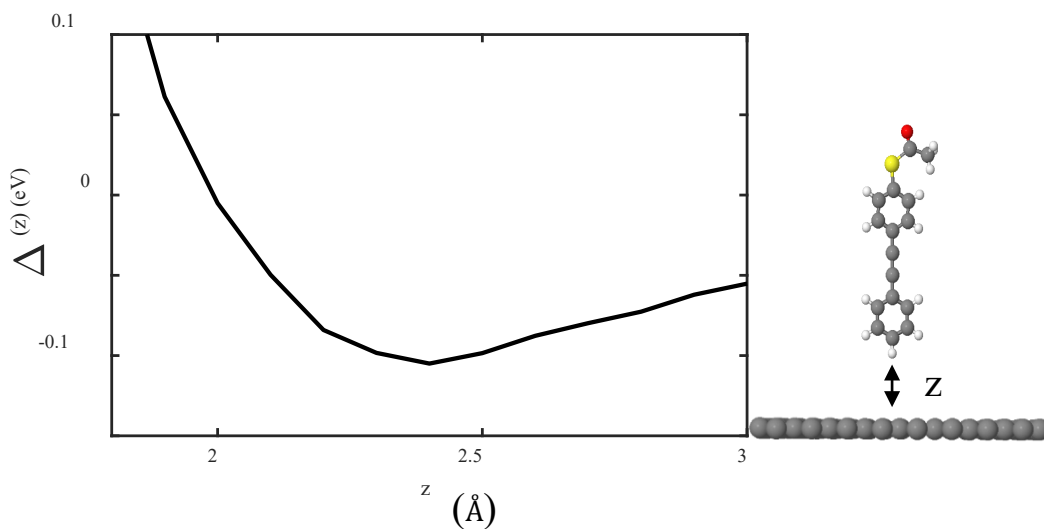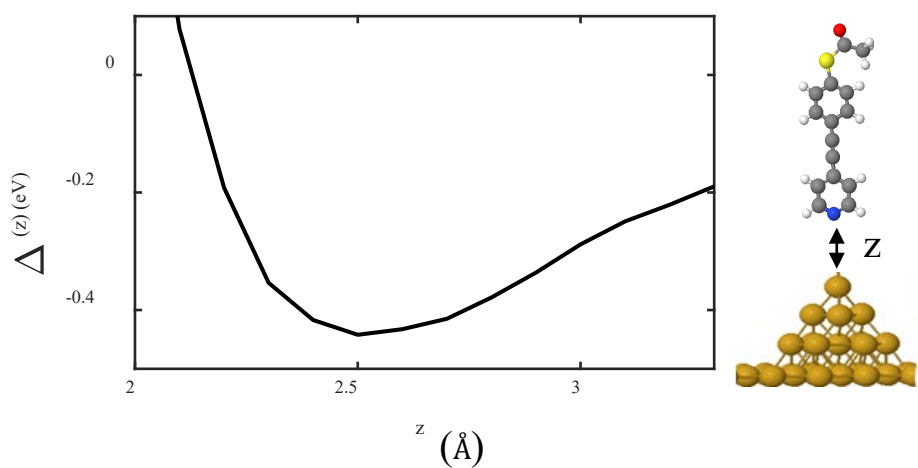
Fig. S23. Phenyl ring (molecule **1**) on a graphene surface (Right panel). Energy difference of phenyl anchor to graphene as a function of molecule-contact distance. The equilibrium distance corresponds to the energy minimum and is found to be approximately 2.4 Å (Left panel).
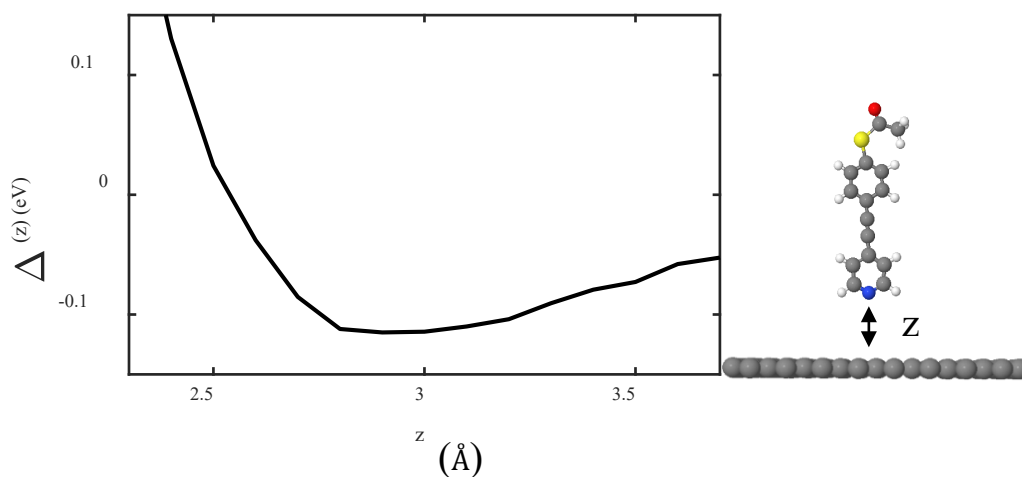
Fig. S24. Pyridine anchor (molecule **2**) on a graphene surface (Right panel). Energy difference of pyridine anchor to graphene as a function of molecule-contact distance. The equilibrium distance is approximately 2.7 Å (Left panel).
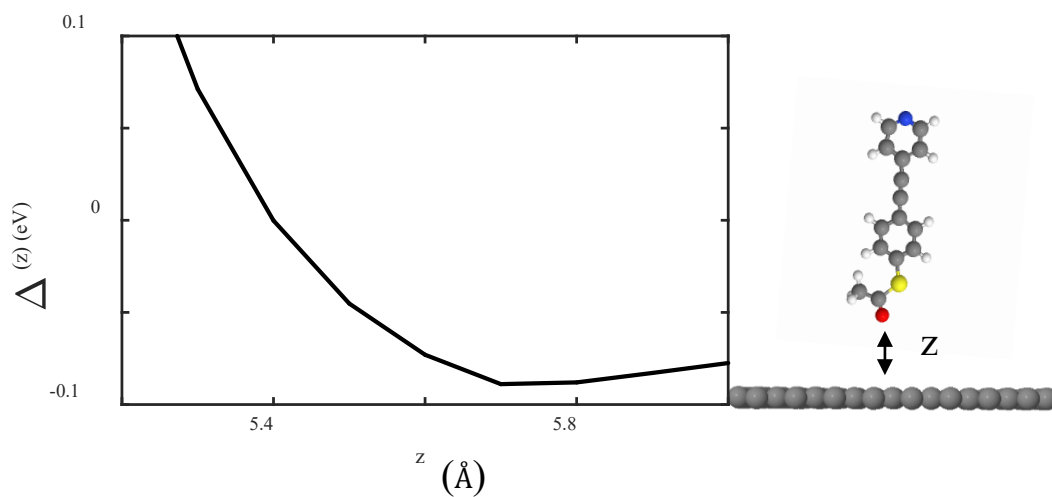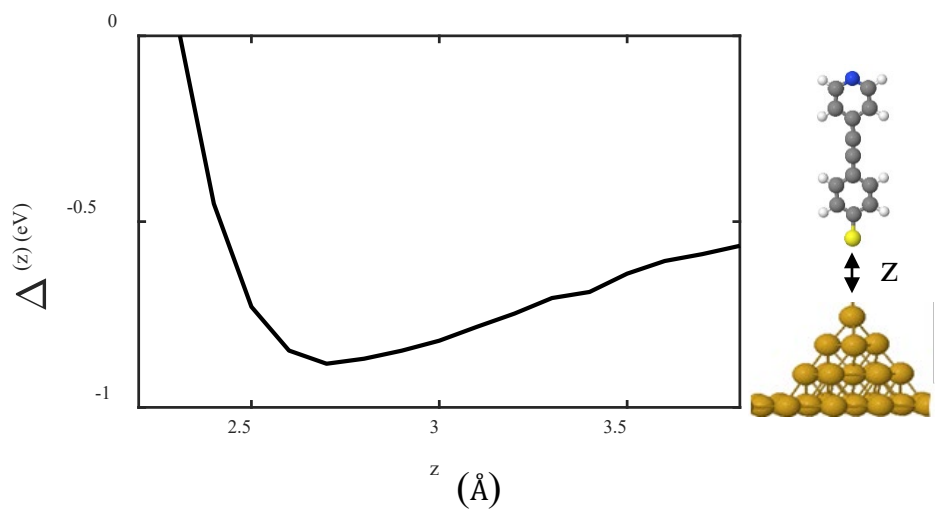
Fig. S25. Thioacetate anchor (molecule **2**) on a graphene surface (Right panel). Energy difference of thioacetate anchor to graphene as a function of molecule-contact distance. The equilibrium distance is approximately 5.7 Å (Left panel).
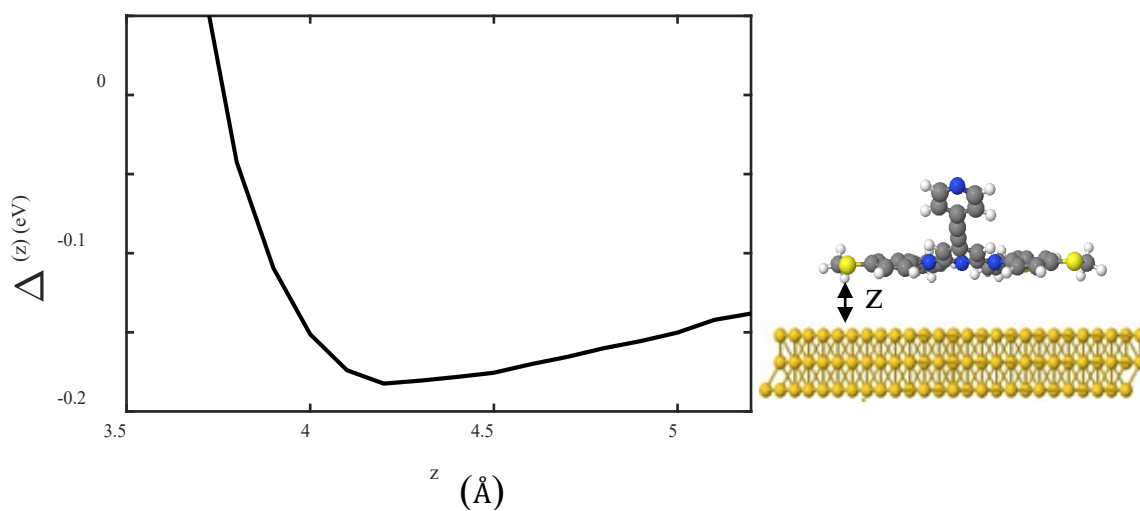

Fig. S26. Pyridine anchor (molecule **2**) on a gold surface (Right panel). Energy difference of pyridine anchor to gold as a function of molecule-contact distance. The equilibrium distance is approximately 2.5 Å (Left panel).

Fig. S27. Thiolate anchor (molecule **2**) on a gold surface (Right panel). The acetyl protecting group has been released. Energy difference of thiolate anchor to gold as a function of molecule-contact distance. The equilibrium distance is approximately 0.27 nm (Left panel).


Fig. S28. Thiomethyl anchor (molecule **6**) on a flat gold surface (Right panel). Energy difference of 4 thiomethyl anchors to flat gold as a function of molecule-contact distance. The equilibrium distance is approximately 4.2 Å (Left panel).

Compound	$\Delta(z)$ (eV)	z (Å)
Gr-Phenyl	0.11	2.4
Gr-Pyridine	0.14	2.7
Gr-Thioacetate	0.09	5.7
Au-Pyridine	0.42	2.5
Au-Thiol	0.85	2.7
Au-Thioether	0.20	4.2

Table S5: Summary of the energy-difference calculations (Figs. S22-S27) for graphene-molecule (Gr-M) and gold-molecule (Au-M) contacts. z is the equilibrium distance and $\Delta(z)$ is the corresponding minimum energy difference.

2.4 Optimized DFT structures of compounds within their junctions

Using the optimized structures and geometries for the compounds obtained as described above, we again employed the SIESTA code to calculate self-consistent optimized geometries, ground-state Hamiltonians and overlap matrix elements for each graphene-molecule-gold junction. The optimized structures were then used to compute the transmission curve for each compound. The DFT-optimized geometries are shown in Fig. S29. Note that there is a tilt-angle range for each compound, which is presented in section 2.5.
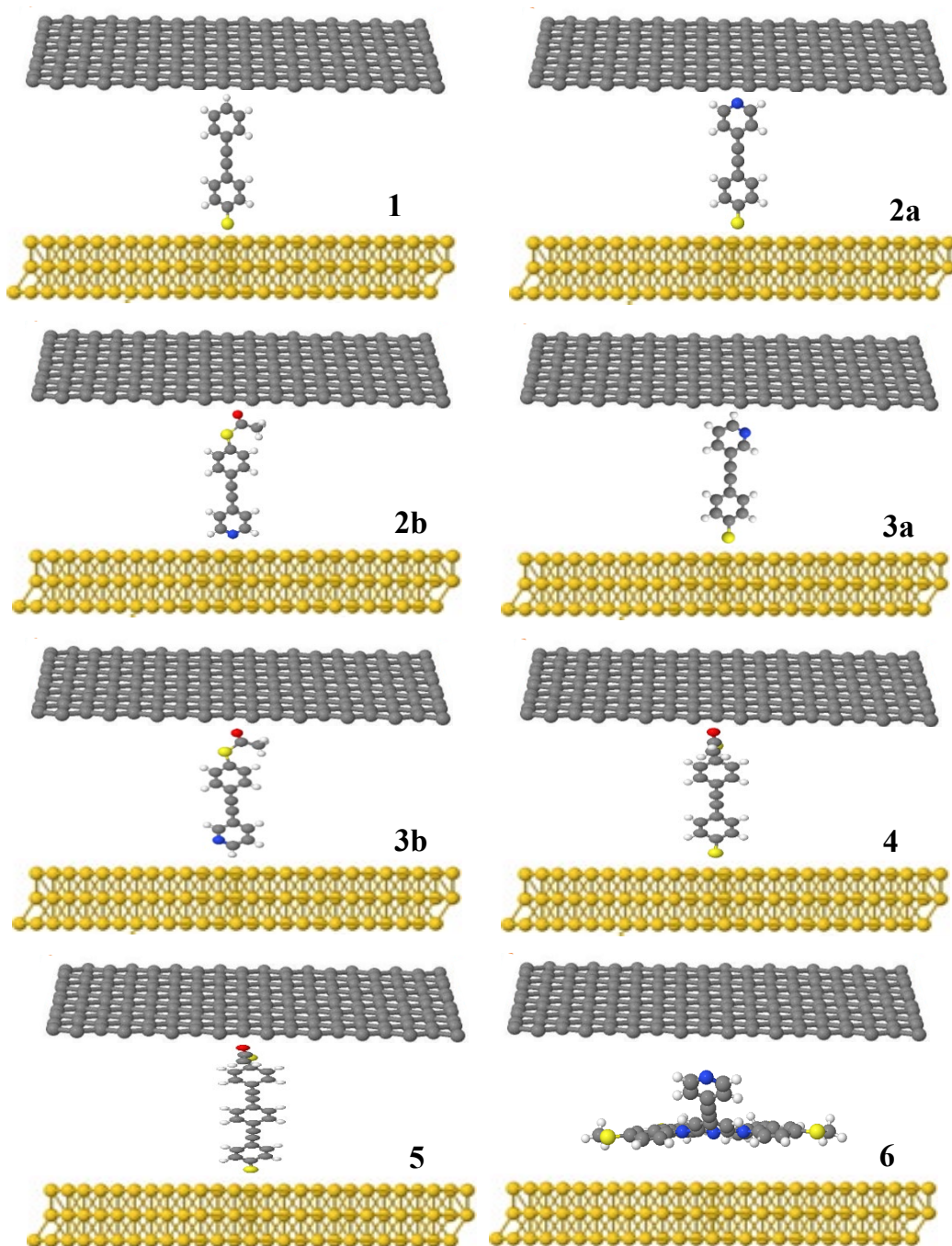
Fig. S29. Schematic illustration of junctions containing a single molecule **1-6**. (The nomenclature a and b for molecules **2** and **3** refers to the binding motif, as in manuscript Figure 2). The top contact is single-layer graphene (SLG) and the bottom contact is gold.
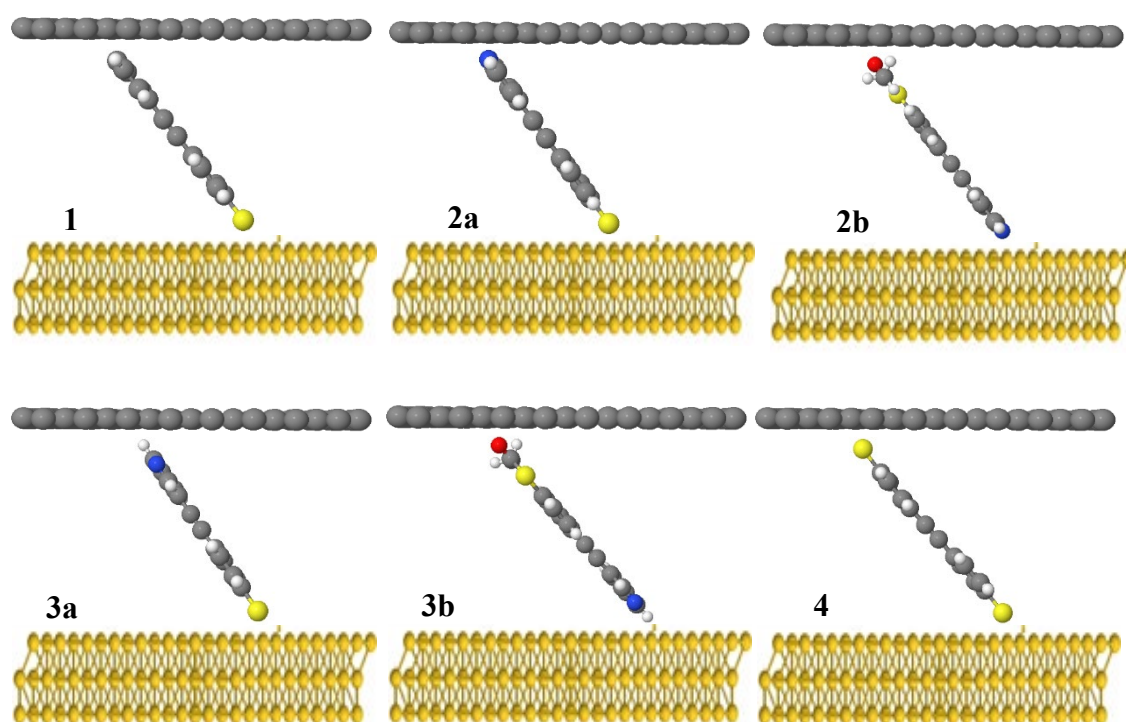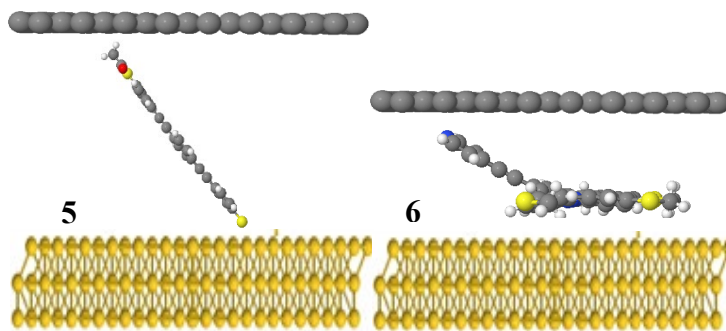
2.5 Tilt angle

In this section, we determine the tilt angle θ of each compound and binding motif between SLG and a gold substrate, which corresponds to the experimentally measured most-probable break-off distance. Table S6 shows a range of tilt angles calculated from the film thickness for each molecule. Break-off distance values suggest that compounds **1**, **2a**, **3a**, **3b**, **4, 5** and **6** tilt at an angle θ ranging from 37° to 47° and compound **2b** tilts at 63° to 73°, as shown in Fig.

S30.

Compound and binding motif	Experimental film thickness (nm)	Equivalent experimental tilt angle (θ)	Equivalent theoretical tilt angle (θ)
1	0.8	37°-47°	37°-47°
2a	1.05	37°-47°	37°-47°
2b		63°-73°	63°-73°
3a	0.7	37°-47°	37°-47°
3b		12°-20°	12°-20°
4	1.1	37°-49°	37°-49°
5	1.7	35°-55°	35°-55°
6	0.8	35°-45°	35°-45°

Table S6: Experimental break-off distances and equivalent tilt angles (θ)

**Fig. S30.** Tilt angle of structures **1**-**6**.

2.6 DFT-based transport calculations

In the following transport calculations, the ground-state Hamiltonian and optimized geometry of each compound was obtained using the density-functional theory (DFT) code.[10] The local-density approximation (LDA) exchange-correlation functional was used along with double-zeta-polarized (DZP) basis sets and the norm-conserving pseudo-potentials. The real-space grid was defined by a plane-wave cut-off of 250 Ry. Geometry optimization was carried out to a force tolerance of 0.01 eV/Å. This process was repeated for a unit cell with the molecule between graphene and gold electrodes where the optimized distances between SLG/Au and the anchor groups are shown in Table S5. From the ground-state Hamiltonian, the transmission coefficient, and hence the room-temperature electrical conductance G, were obtained as described in the sections below. We modelled the properties of a single molecule in the junction, as previous works[14] have shown that the calculated conductance per molecule of a SAM differs only slightly from that of single molecules.

## 2.7 Transport calculations in a three-terminal junction

To calculate the electrical transport through a SAM (**1-6**), we modelled the three-terminal junction shown in the top panel of Fig. S31. The in-plane periodicity of the graphene and the molecular layer is achieved by repeating the unit cell using a Bravais lattice with 50k points in the *y*-direction (see upper black arrow). The gold electrode is modelled as a nanowire attached to each molecule. A mean-field Hamiltonian and an overlap matrix were extracted from the converged DFT calculation and combined with our quantum-transport calculation code, Gollum, to calculate the transmission coefficient *T*(*E*) of electrons of energy *E* passing from the graphene to the gold electrode.

In the three-terminal junction, there are two transmission functions 1-3 and 2-3 describing transport between the gold and graphene electrodes.
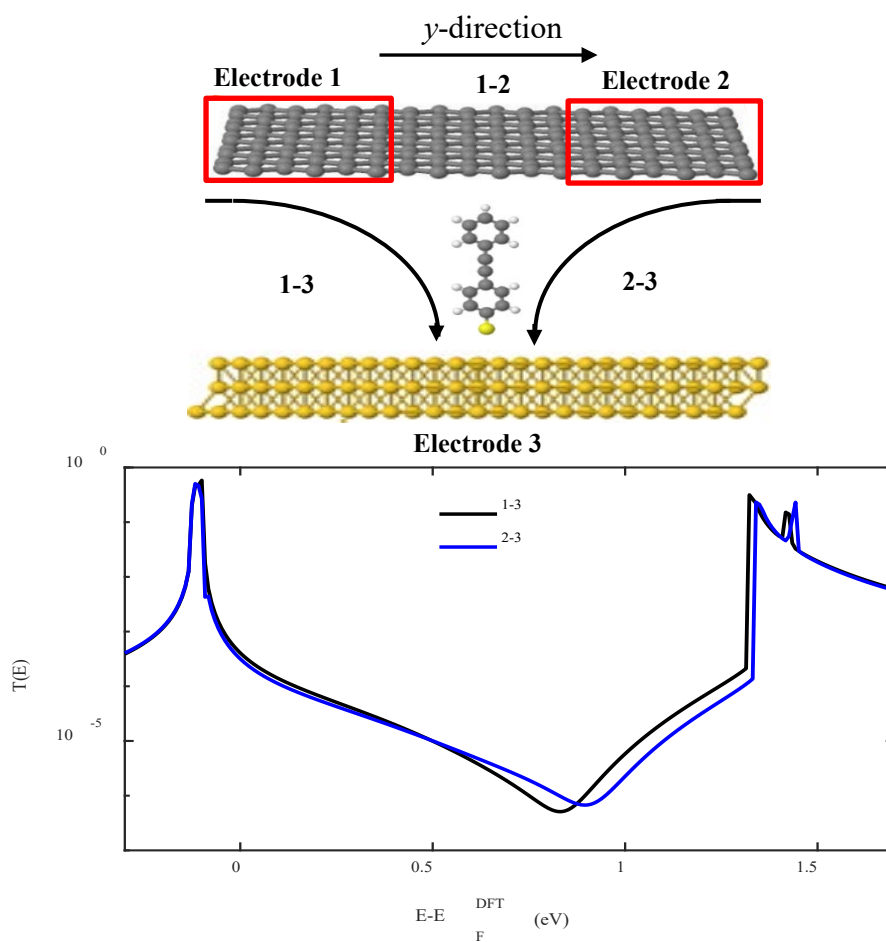
Fig. S31. Top panel: schematic illustration of a three-terminal Au/**1**/SLG junction with periodic boundary conditions along the *y*-axis. The top contact is SLG and is divided into two electrodes (electrode 1 and electrode 2), whereas the bottom contact is Au (electrode 3). Bottom panel: an example of zero-bias transmission coefficient *T*(*E*) curves: 1-3 and 2-3 have equal path lengths, and therefore have identical curves (black and blue lines).

Since the two paths 1-3 and 2-3 yield almost identical transmission coefficients *T*(*E*), the average of them is shown in Figures S32-S37. Fig. S32 shows the average transmission coefficient *T*(*E*) for SAM **1**, whose tilt angle is 40º.
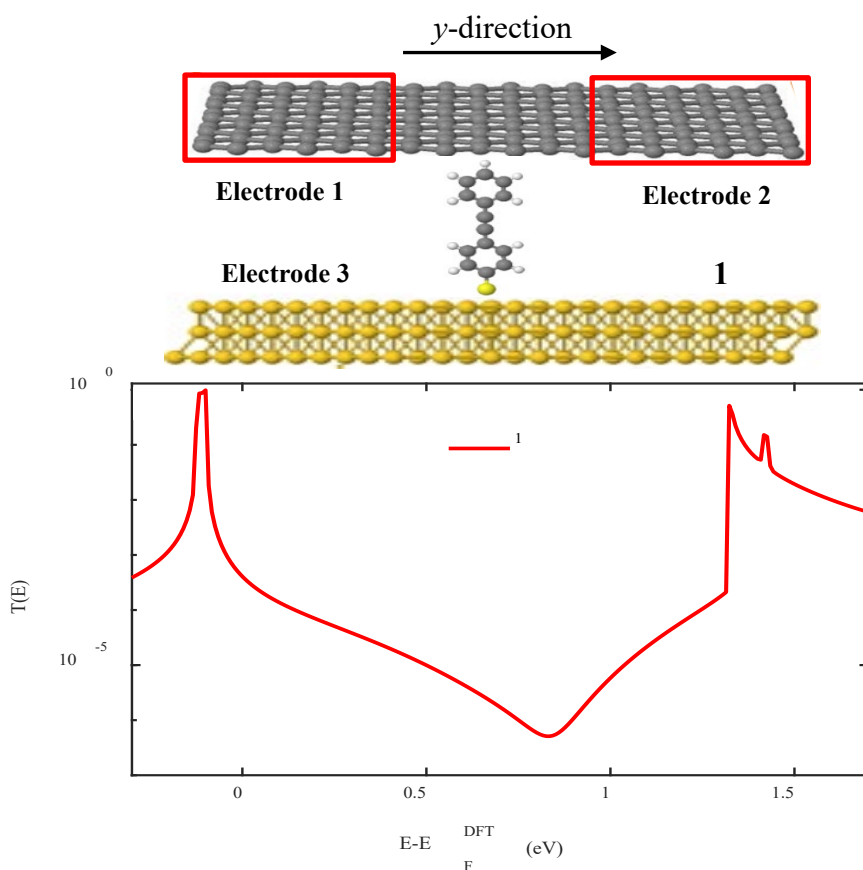
Fig. S32. Top panel: schematic illustration of a three-terminal Au/**1**/SLG junction with periodic boundary conditions along the *y*-axis, as in Fig. S31. Bottom panel: zero-bias transmission coefficient *T*(*E*) averaged over the values for paths 1-3 and 2-3 shown in Fig. S31.

As shown in the upper panel of Fig. S33, for **2**, there are two possible binding configurations (motifs) in the junction. For **2a** the (deprotected) thiolate binds to Au and pyridine binds to SLG, and for **2b** the molecule is flipped vertically in the junction, with the pyridine binding to the gold and the (protected) thioacetate to the SLG. As expected **2b** yields lower conductance (bottom panel), because the separation between the Au and SLG electrodes is larger than in **2a**.
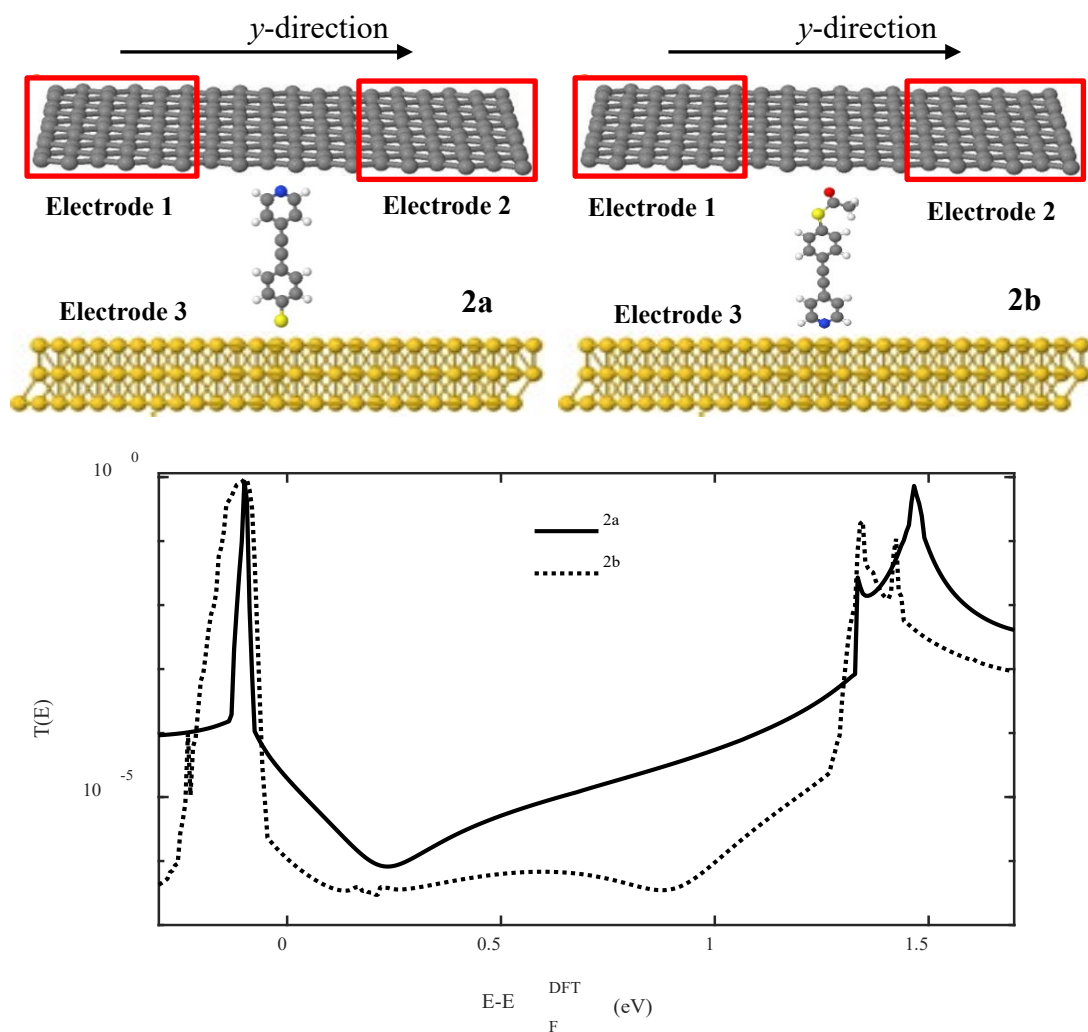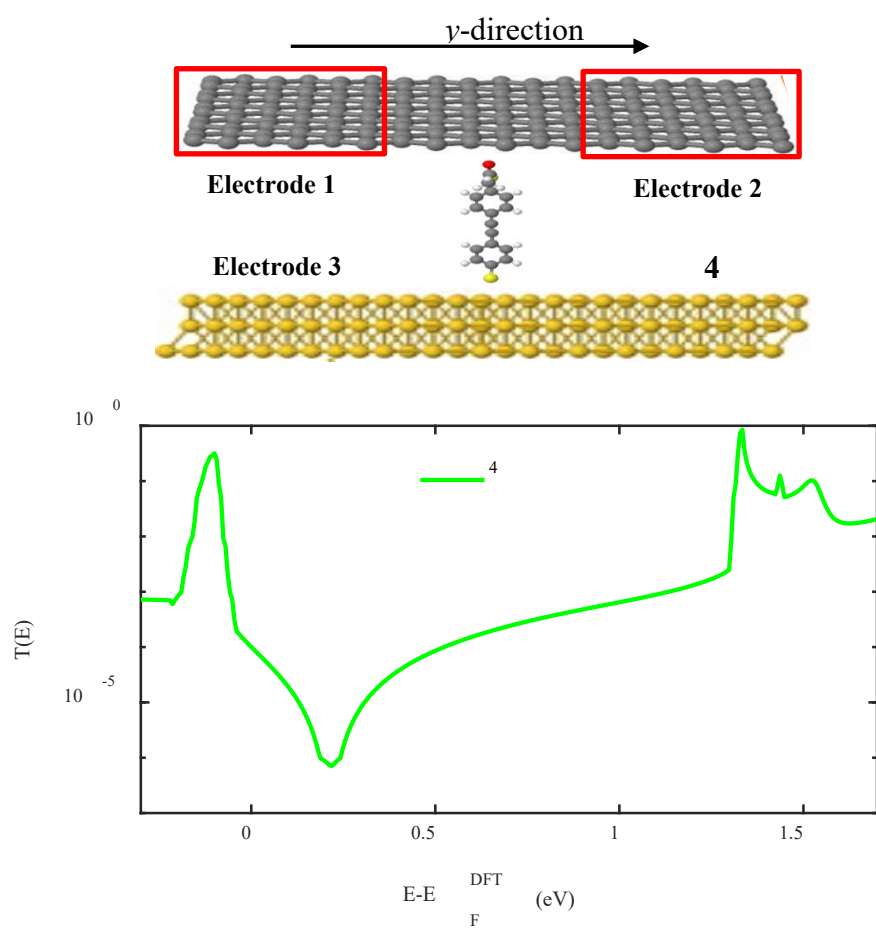
Fig. S33. The same as Fig. S31 for three-terminal Au/**2a** or **2b**/SLG junctions.

Similarly, **3** also has two possibilities in the junction. Configuration **3a** occurs when the thiolate binds to Au and pyridine binds to SLG, and **3b** when the molecule is flipped vertically in the junction, with the pyridine binding to Au and the thioacetate to the SLG as shown in the top panel of Fig. S34. **3b** yields a lower conductance (bottom panel), because the separation between the Au and SLG electrodes is larger than in **3a**.
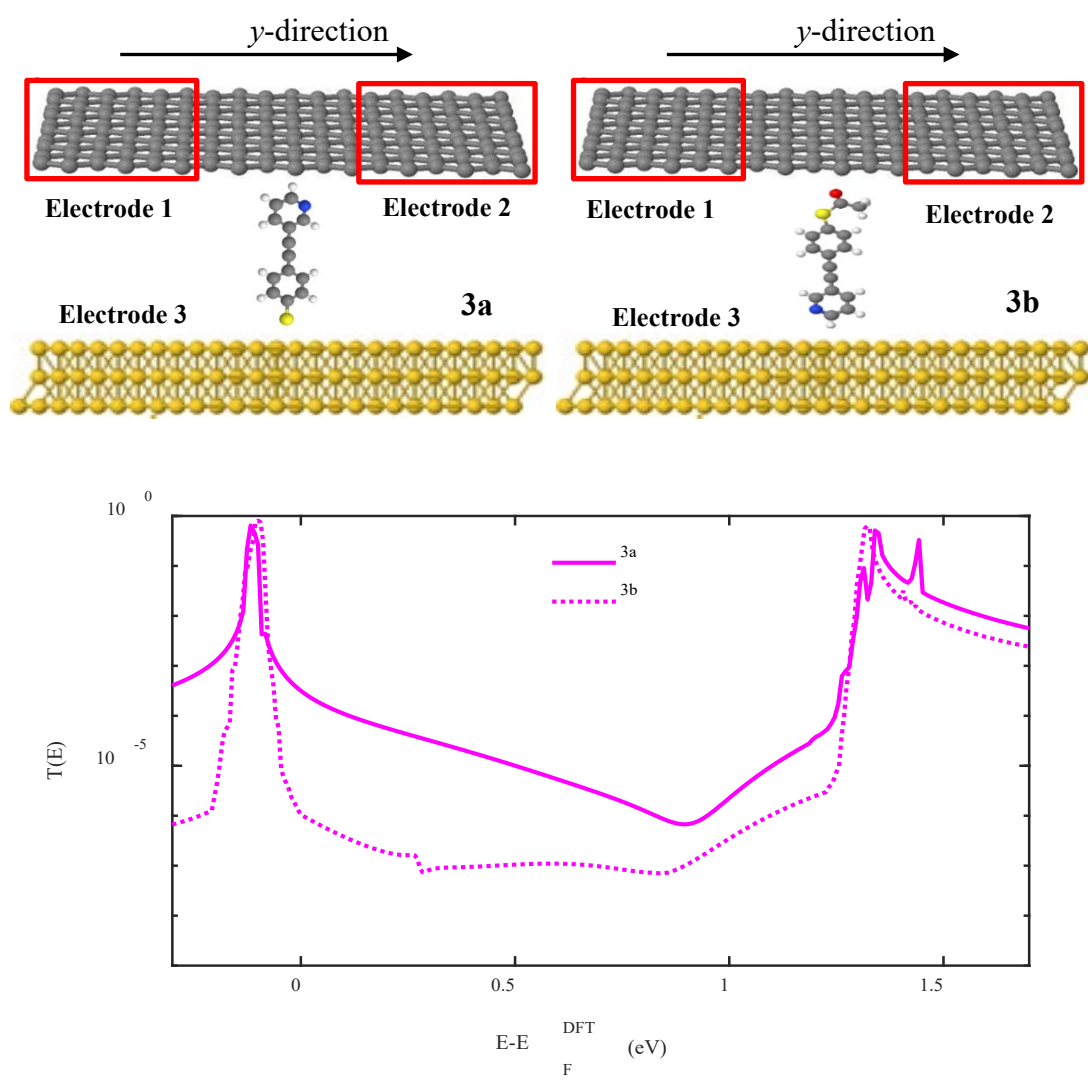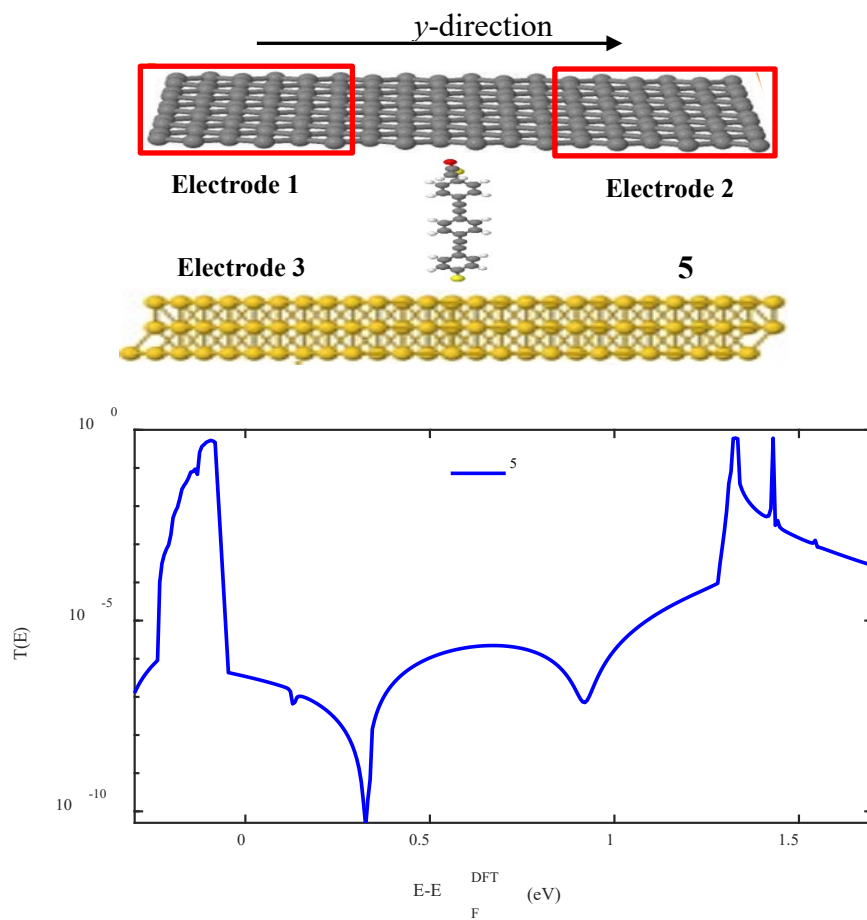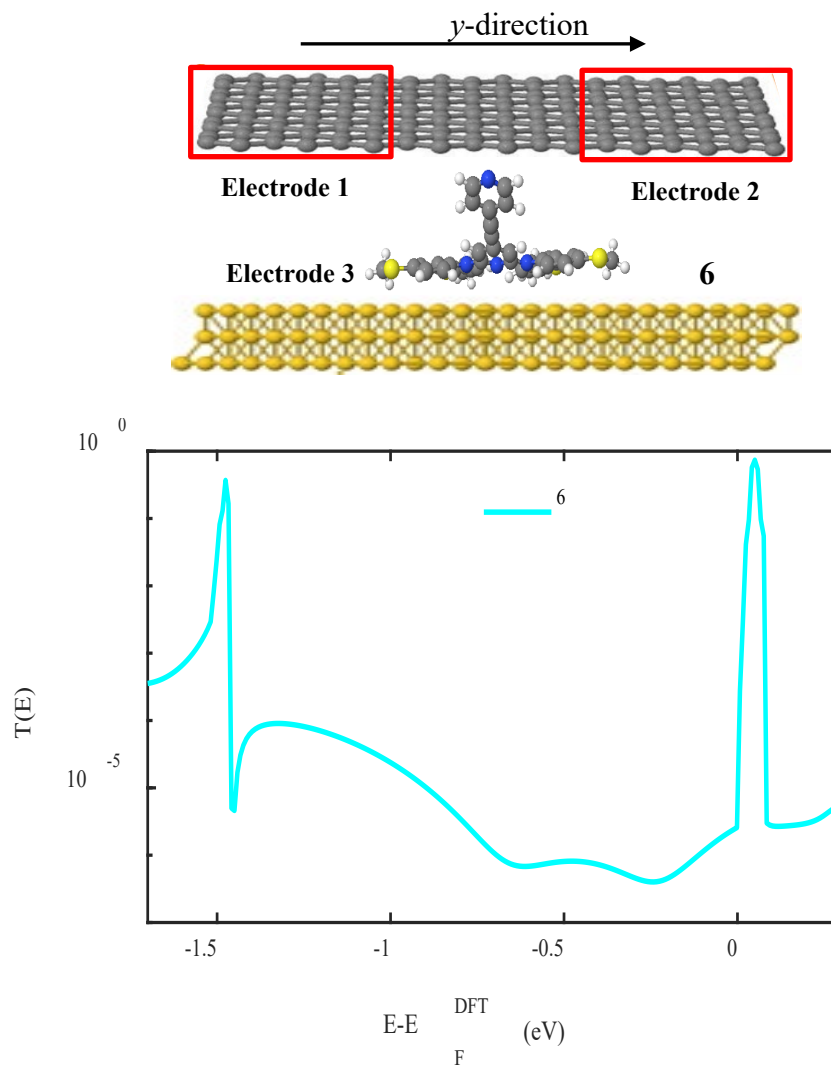
Fig. S34. The same as Fig. S31 for three-terminal Au/**3a** or **3b**/SLG junctions.

Fig. S35. The same as Fig. S31 for a three-terminal Au/**4**/SLG junction.

y-direction

Electrode 1

Electrode 2

Electrode 3

5

T(E)

$E-E_F^{DFT}$ (eV)

Fig. S36. The same as Fig. S31 for a three-terminal Au/**5**/SLG junction.

Fig. S37. The same as Fig. S31 for a three-terminal Au/**6**/SLG junction.

The HOMO resonance is predicted to be pinned near the Fermi Level of the electrodes for molecules **1-5** as shown in Fig. S38a. In contrast, the LUMO resonance is predicted to be pinned near the Fermi Level of the electrodes for **6** as shown in Figure S38b.
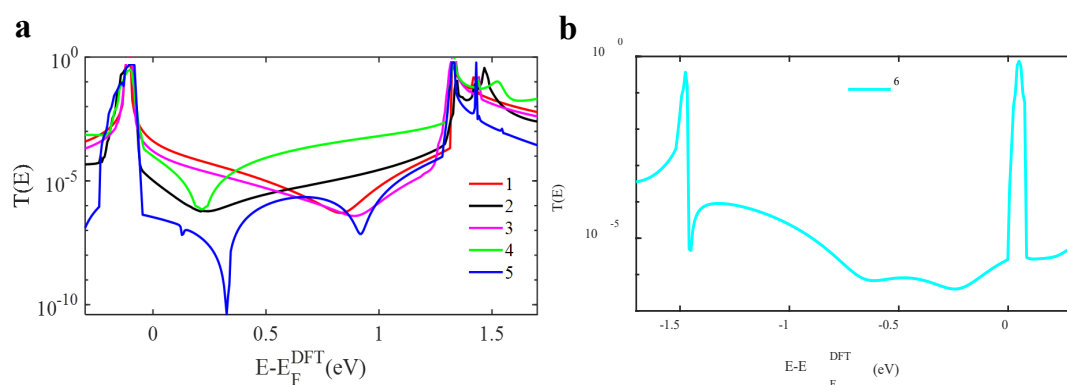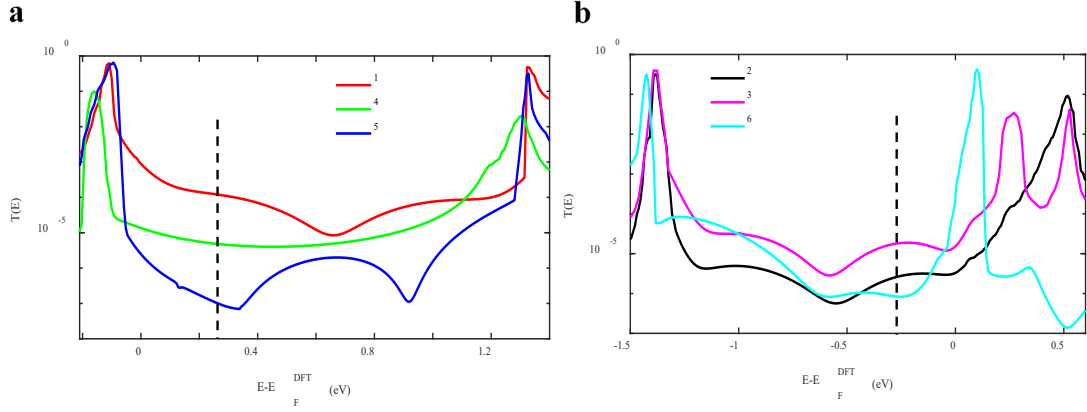
Fig. S38. **a:** Zero-bias transmission coefficient $T(E)$ of molecules **1-5** as a function of energy. The HOMO resonance is predicted to be pinned near the DFT-predicted Fermi energy. **b:** The zero-bias transmission coefficient $T(E)$ of **6**, reproduced from Fig. S37. The LUMO resonance is predicted to be pinned near the DFT-predicted Fermi energy (flat Au substrate).

The above transmission-function calculations (Fig. S38) were repeated with the molecules bound to a gold atomic cluster rather than a flat Au substrate, as shown in Fig. S39. Figure S40 demonstrates that the position of E_F in 4 molecules (**1**, **4–6**) is unaffected by the shape of the Au electrode whereas in molecules **2** and **3** E_F moves from being close to the HOMO to near the LUMO when the Au substrate is changed from flat gold to a cluster of gold on the substrate (see Figs. S38 and S40).
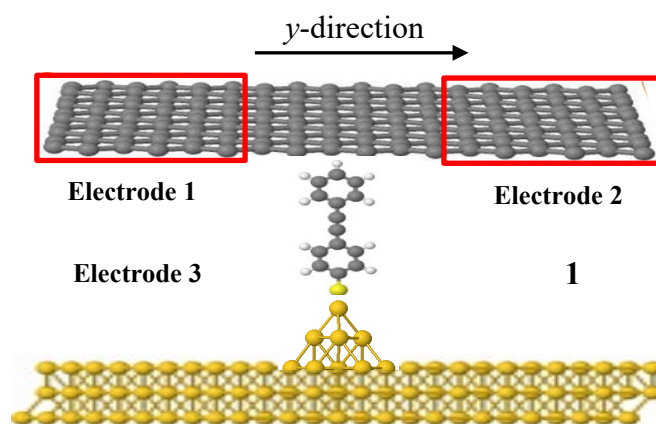
Fig. S39. Schematic illustration of a three-terminal Au/**1**/SLG junction with periodic boundary conditions along the *y*-axis. The top contact is SLG and is divided into two electrodes (electrodes 1 and 2), whereas the bottom contact (electrode 3) has a cluster of Au atoms.

37

Fig. S40. **a:** Zero-bias transmission coefficient $T(E)$ of molecules **1, 4** and **5** as a function of energy. The HOMO resonance is predicted to be pinned near the DFT-predicted Fermi energy. **b:** Zero-bias transmission coefficient $T(E)$ of **2, 3** and **6**. The LUMO resonance is predicted to be pinned near the DFT-predicted Fermi energy (cluster of gold atoms). The vertical dashed lines show the values of the Fermi energy used in Table 1 of the main text and in Fig 5. For **1, 4, 5** the Fermi energy is close to the HOMO. For **3, 6** it is close to the LUMO and for **2** it is close to the mid gap.

To model the periodicity in the graphene, the unit cell was repeated using a Bravais lattice with 50 k-points in the y-direction. The mean-field Hamiltonian and overlap matrix were extracted from this converged calculation. To model the source-drain and gate voltages in the experiment, the gold Fermi energy (E_F^{Gold}) is defined to be the zero of energy and is not affected by the source-drain or gate voltages. However, the Fermi energy of the graphene is a function of the source-drain and gate voltages via the equation:

$$E_F^{Gr}\ (V_{SD}, V_G) =\ E_F^{Gold} -\ \alpha V_{SD} - \beta V_G\ , \tag{S2}$$

where V_{SD} and V_G are the source-drain and gate voltages and α and β are related to the experimental lever arms. Similarly, applying a gate voltage can move the energy levels of the molecule up/down in energy:

$$\varepsilon^{HOMO}(V_G) =\ \varepsilon_m^{HOMO} - \Upsilon_G V_G\ , \tag{S3}$$

$$\varepsilon^{LUMO}(V_G) =\ \varepsilon_m^{LUMO} - \Upsilon_G V_G\ . \tag{S4}$$

Υ_G is a scaling parameter used to match the data. The current is then given by

$$I(V_D, V_G) = \frac{2e}{h}\ \int_{E_F^{Gold}}^{E_F^{Gr}} T(E, V_{SD}, V_G)\ dE \tag{S5}$$

where $T(E, V_D, V_G)$ is the transmission coefficient from lead 1 to lead 3 calculated using the quantum transport code GOLLUM.[75] It is assumed that the energies of the molecular levels relative to E_F^{Gold} are independent of V_D and that positive (negative) bias voltage decreases (increases) the Dirac point relative to E_F^{Gold} (Eq. S2). The current is computed using Eq. S5 by evaluating individual transmission coefficients $T(E, V_D, V_G)$ at every V_D and computing the associated current. dI/dV_D curves were then obtained by differentiating the current with respect to V_D.

Finally, we provide a 2D plot of $\log(G)$ versus V_G and V_{SD} for molecules **1-6** (a-f), for a wide range of $V_{SD} = \pm 0.5$ as shown in the left panel of Fig. S41. Comparing the conductance ratio between the theory and experiment on the colour bar of $\log(G)$, it is found that the theoretical ratio is higher than in the experiment (right panel). Theory plots (left panel), have been replotted with a smaller range of $V_{SD} = \pm 0.1$, in Figure 5 in the manuscript. It should be noted that the vertical heights of the diamonds for molecule **2** in Fig S41 and Fig. 5 are a consequence of the colour scale adopted and do not coincide with the HOMO-LUMO gap.
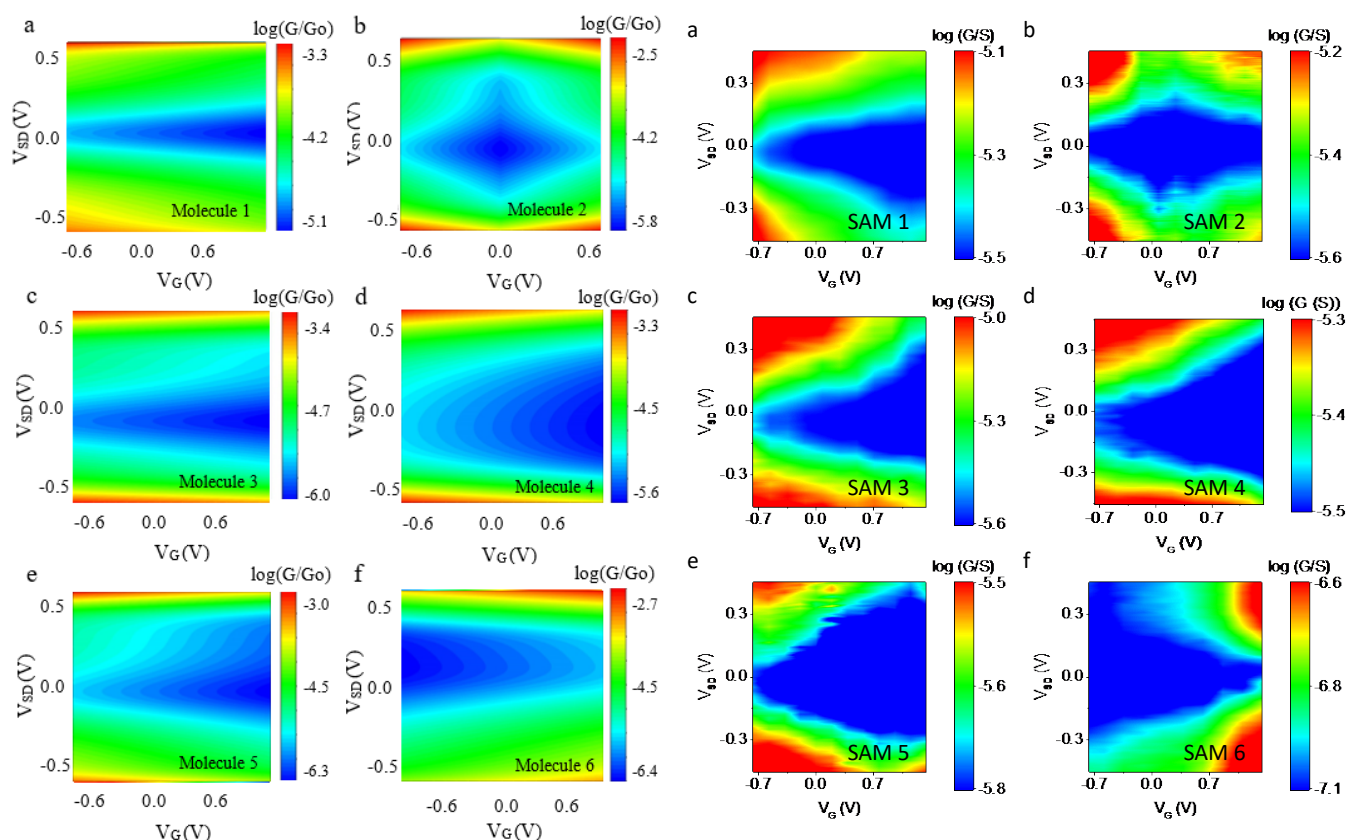
Fig. S41. Comparison between theory and experiment of $\log(G)$ vs. V_G and V_{SD} for SAMs **1-6** (theory left panel and experiment right panel)
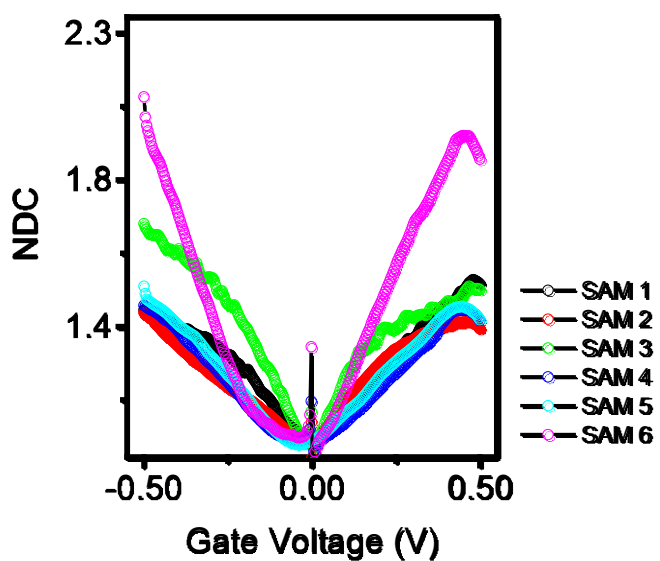
Fig. S42. Normalized differential conductance (NDC) curves for SAMs **1-6.**
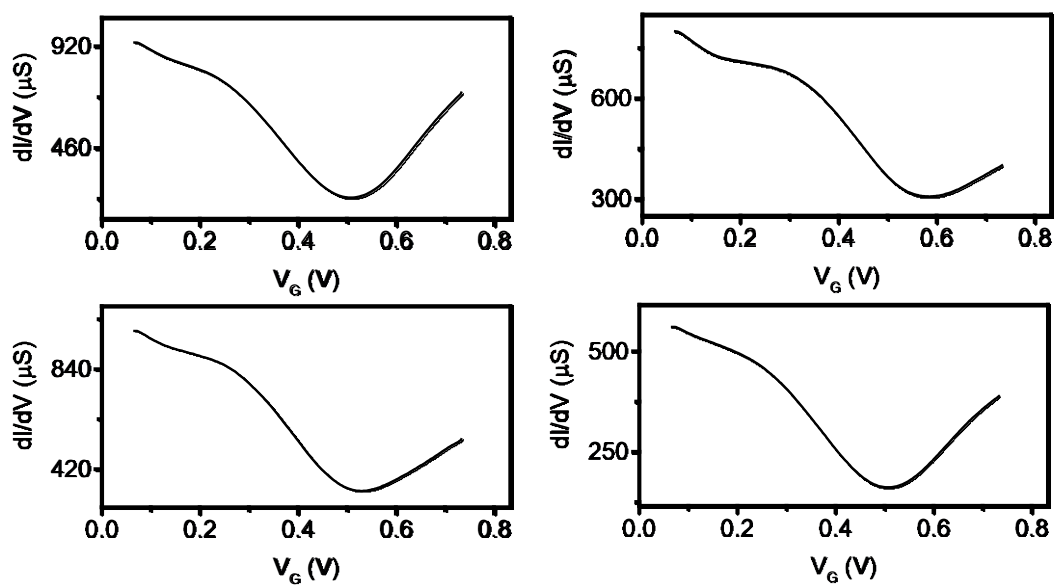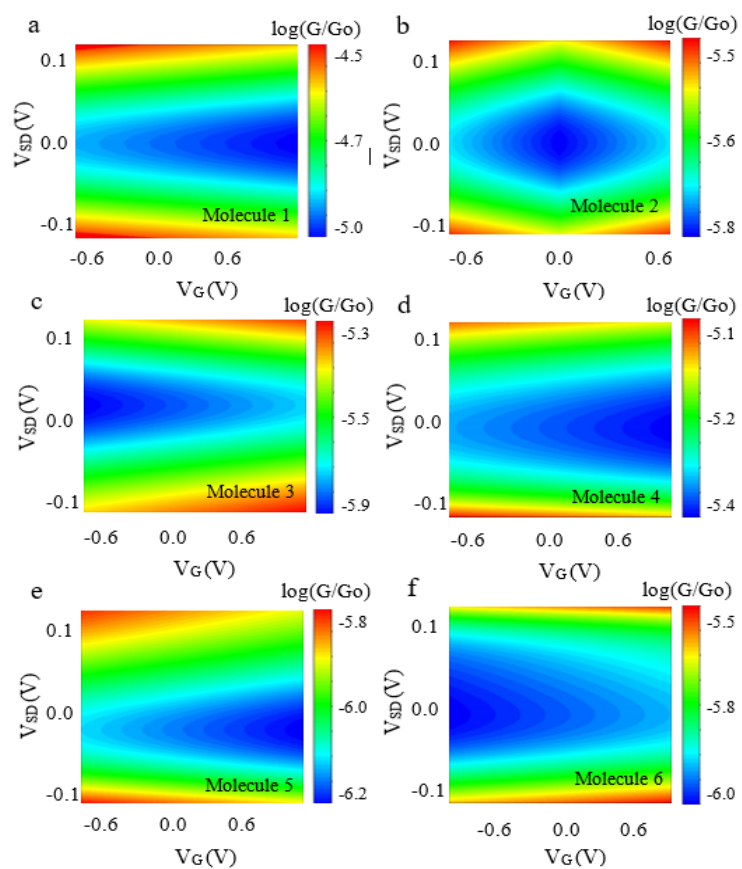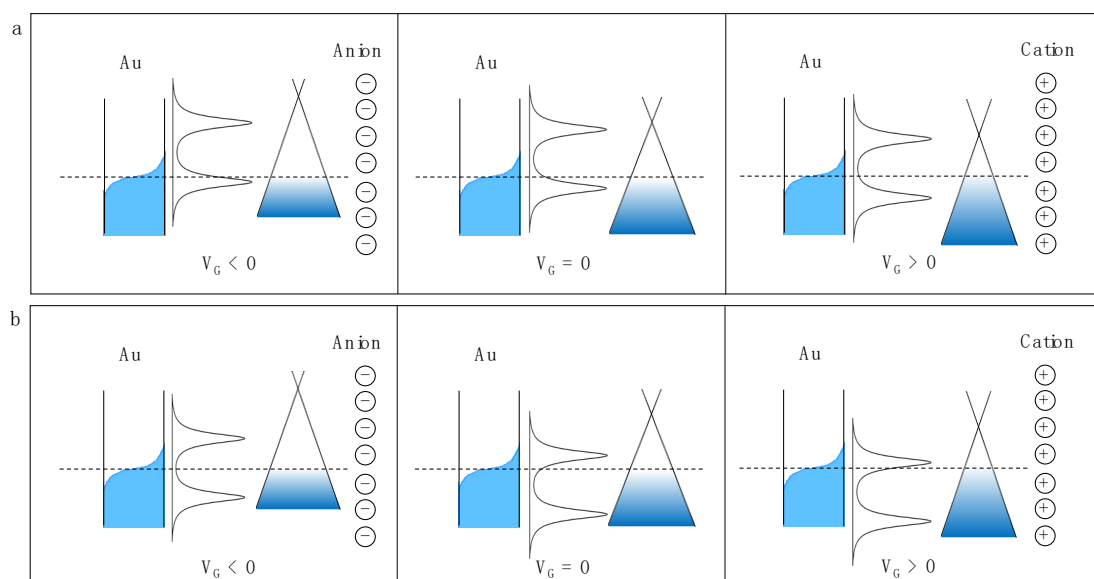

Fig. S43. Gate-conductance response of 4 devices with graphene only, graphene prepared by same method, but from different batches. The data show good reproducibility and the positive value of V_G shows the graphene is p-doped.

Fig. S44. Theoretical plots of V_G vs. V_{SD} vs. log (G) for molecules **1-6** (a-f, respectively).

Fig. S45. Energy diagram of a HOMO and LUMO dominated molecule with different gate voltages on the ionic liquid

References

1. L. J. O'Driscoll, X. Wang, M. Jay, A. S. Batsanov, H. Sadeghi, C. J. Lambert, B. J. Robinson and M. R. Bryce, *Angew. Chem. Int. Ed.*, 2020, **59**, 882-889.

2. V. Kaliginedi, P. Moreno-García, H. Valkenier, W. Hong, V. M. García-Suárez, P. Buiter, J. L. Otten, J. C. Hummelen, C. J. Lambert and T. Wandlowski, *J Am Chem Soc*, 2012, **134**, 5262-5275.

3. N. Stuhr-Hansen, J. K. Sørensen, K. Moth-Poulsen, J. B. Christensen, T. Bjørnholm and M. B. Nielsen, *Tetrahedron*, 2005, **61**, 12288-12295.

4. D. L. Pearson and J. M. Tour, *J Org Chem*, 1997, **62**, 1376-1387.

5. L. J. O'Driscoll, X. Wang, M. Jay, A. S. Batsanov, H. Sadeghi, C. J. Lambert, B. J. Robinson and M. R. Bryce, *Angew Chem Int Ed*, 2020, **132**, 892-899.

6. Z. M. Wei, T. Li, K. Jennum, M. Santella, N. Bovet, W. P. Hu, M. B. Nielsen, T. Bjornholm, G. C. Solomon, B. W. Laursen and K. Norgaard, *Langmuir*, 2012, **28**, 4016-4023.

7. H. Valkenier, E. H. Huisman, P. A. van Hal, D. M. de Leeuw, R. C. Chiechi and J. C. Hummelen, *J Am Chem Soc*, 2011, **133**, 4930-4939.

8. Q. Lu, K. Liu, H. M. Zhang, Z. B. Du, X. H. Wang and F. S. Wang, *Acs Nano*, 2009, **3**, 3861-3868.

9. H. Song, H. Lee and T. Lee, *J Am Chem Soc*, 2007, **129**, 3806-3807.

10. J. M. Soler, E. Artacho, J. D. Gale, A. García, J. Junquera, P. Ordejón and D. Sánchez-Portal, *J Phys: Conden Mat*, 2002, **14**, 2745.

11. E. Artacho, E. Anglada, O. Diéguez, J. D. Gale, A. García, J. Junquera, R. M. Martin, P. Ordejón, J. M. Pruneda and M. Sánchez-Portal, *J Phys: Conden Mat*, 2008, **20**, 064208.

12. A. K. Ismael and C. J. Lambert, *J Mat Chem C,* 2019, **7**, 6578-6581.

13. M. Gantenbein, L. Wang, A. A. Al-Jobory, A. K. Ismael, C. J. Lambert, W. Hong and M. R. Bryce, *Sci Rep*, 2017, **7**, 1794.

14. L. Herrer, A. Ismael, S. Martin, D. C. Milan, J. L. Serrano, R. J. Nichols, C. Lambert and P. Cea, *Nanoscale*, 2019, **11**, 15871-15880.